Impact Factor: 4.4
Q2

Results in Surfaces and Interfaces 23 (2026) 100726

Contents lists available at ScienceDirect

Results in Surfaces and Interfaces

journal homepage: www.elsevier.com/locate/rsurfi

Integrated molecular modelling and eriodictyol SLNs from *Ocimum tenuiflorum*: A promising anti-breast cancer therapeutic with enhanced drug delivery

Salem Salman Almujri [a], Prasanalakshmi Balaji [b], Kumarappan Chidambaram [c], Srinivasan Ramamurthy [d], Malarkodi Velraj [e], Swati Mayur Keny [f], A. Santhana Krishna Kumar [g,**], Panneerselvam Theivendren [h,*]

[a] Department of Pharmacology, College of Pharmacy, King Khalid University, Asir, Abha, 62529, Saudi Arabia
[b] Department of Computer Science, College of Computer Science, King Khalid University, Abha 62521, Saudi Arabia
[c] Department of Pharmacology, College of Pharmacy, King Khalid University, Abha, 62529, Saudi Arabia
[d] Department of Pharmacy, College of Dentistry &Health Sciences, Fujairah University, Fujairah, 2202, United Arab Emirates
[e] Department of Pharmacognosy, School of Pharmaceutical Sciences, Vels Institute of Science, Technology & Advanced Studies, Pallavaram, Chennai, Tamil Nadu, 600117, India
[f] Department of Pharmaceutics, PES's Rajaram and Tarabai Bandekar College of Pharmacy, Ponda, 403401, Goa, India
[g] Department of Chemistry, National Sun Yat-sen University, No. 70, Lien-hai Road, Gushan District, Kaohsiung City, 80424, Taiwan
[h] Department of Pharmaceutical Chemistry & Analysis, School of Pharmaceutical Sciences, Vels Institute of Science, Technology & Advanced Studies, Pallavaram, Chennai, Tamilnadu, 600117, India

ARTICLE INFO

Keywords:
Eriodictyol
Breast cancer
Solid lipid nanoparticles
Molecular dynamics
Drug delivery

ABSTRACT

In this work, machine-learning prediction, molecular modelling and nanocarrier development are used to assess Eriodictyol of *Ocimum tenuiflorum* as a possible anti-breast-cancer treatment against the progesterone receptor (PR). A BindingDB curated dataset was modelled with the aid of a variety of algorithms, and the best results were obtained with Rand Forest (accuracy 78.12, kappa 0.5361). Molecular docking predicted the presence of affinity of binding at −14.4 kcal/mol and rich interaction profile comprising six hydrogen bonds, three hydrophobic contacts, and a p-p stacking interaction with the key residues GLN725, MET756, LEU715, LEU718 and also PHE778. The stability of the complex was verified through molecular dynamics (100 ns, OPLS-2005 force field, 300K) where the protein RMSD error stayed within 1.0-1.6 A, and high hydrogen-bond occupancy (LEU715: 0.90; LEU718: 0.85). MM-GBSA analysis had produced a good binding free energy of −51.00 kcal/mol. The solid lipid nanoparticles (SLNs) loaded with erythrolictol showed good physicochemical characteristics such as; 90% encapsulation efficiency, loading capacity of 9.7, particle size of 120-130 nm and zeta potential of −30 mv. The pH-responsive release was noted (95 and 63 percent at pH 7.4 and pH 5.1, respectively) which followed the first-order reaction ($r^2 = 0.981$). Cytotoxicity tests revealed that it had a dose dependent inhibition with IC_{50} of 37.2 μg/mL. In general, the combined results can justify Eriodictyol-SLNs as a potential therapeutic agent in breast cancer.

1. Introduction

Cancer is a significant global health issue today with an estimated ten million deaths annually and second only to heart disease as the leading cause of death. According to the estimations of the International Agency of Research on Cancer, the global incidence will reach 28.4 million cases by 2040, i.e., the increase by 47 per cent, compared with 2020 [1–3]. This alarming tendency can be explained by the ageing of population, changes in lifestyles, exposure to the environment and diagnostic technologies. Essentially, the pathophysiology of cancer rests on the loss of

* Corresponding author. School of Pharmaceutical Sciences, Vels Institute of Science, Technology & Advanced Studies, Pallavaram, Chennai, Tamilnadu, 600117, India.
** Co-corresponding author.
E-mail addresses: krishnakumar@mail.nsysu.edu.tw (A. Santhana Krishna Kumar), tpsphc@gmail.com (P. Theivendren).

https://doi.org/10.1016/j.rsurfi.2026.100726
Received 22 January 2026; Accepted 26 January 2026
Available online 14 February 2026

normal cell regulatory pathways leading to uncontrolled growth, invasion and metastasis. The complexity of the oncological management is demonstrated by the presence of more than 200 known malignancies with various molecular signatures, variable therapeutic responses, and variable prognoses [4].

The major malignancy in women worldwide is breast cancer with an estimated 2.3 million new cases per year or 24.5% of the total number of female malignancies. The disease is characterised by a high degree of molecular heterogeneity and is divided into subtypes: luminal A and B, HER2-enriched and triple-negative breast cancer, each of which requires different treatment approaches. Breast cancer is a deadly disease that kills over 685,000 people each year across the globe, despite tremendous efforts to detect and treat the disease early. Besides the mortality data there exists a socioeconomic cost to women in their most productive years of life and high health care expenses to societies, especially in resource-starved environments, where access to state-of-the-art treatment is limited [5–7].

The need to treat breast cancer stems from intrinsic limitations in the current therapeutic paradigms. Conventional surgical, chemotherapy, radiotherapy and targeted agent modalities are often accompanied by significant adverse effects, development of drug resistance, tumor recurrence and limited efficacy in metastatic disease. Chemotherapy-related toxicities include cardiotoxicity, neuropathy, myelosuppression, and secondary malignancies, which significantly reduce the quality of life of patients. Moreover, the development of multidrug resistance mechanisms provides an insurmountable obstacle, reinforcing the need for innovative therapeutic strategies that can provide better efficacy and safety [8–10].

Historically, natural products have been the invaluable sources of anticancer agents, accounting for approximately 60% of currently approved oncological therapeutics. Natural products offer unique benefits such as structural diversity, multi-target mode of action, synergistic interactions, and usually a favourable toxicity profile compared to synthetic analogues. Their anticancer activities range over a spectrum of mechanisms including apoptosis induction, cell-cycle arrest, anti-angiogenesis, metastasis inhibition, immune modulation and chemo sensitization [11–13].

Ocimum tenuiflorum, a sacred plant in the traditional medicinal systems, is rich in bioactive phytochemicals as reported to possess a wide range of anticancer properties [14]; [15]. Extracts and isolated constituents from this plant have antiproliferative activity against different malignancies including breast cancer through mechanisms of apoptosis induction, cell-cycle modulation, and blockade of inflammatory pathways. Current studies indicate that *Ocimum tenuiflorum* constituents have the ability to sensitize cancer cells to conventional therapies while providing cytoprotection of normal tissues [16]; [17].

Eriodictyol, the principal flavanone of *Ocimum tenuiflorum*, has been reported to be an excellent anticancer agent for breast cancer. This bioactive compound has demonstrated important therapeutic potentials through a variety of mechanisms, including antiproliferative, apoptotic, antiangiogenic and metastatic inhibition. The authors conclude that Eriodictyol selectively targets breast-cancer stem cells and that it overcomes drug resistance and sensitizes conventional chemotherapy through modulation of key signaling pathways such as PI3K/Akt, NF-kB, and p53 pathways [18]; [19].

The primary goal of this most elaborate investigation was to assess in a systematic manner, the anticancer activity of Eriodictyol isolated from *Ocimum tenuiflorum* against breast cancer in the context of multi-dimensional analytical and biological evaluation framework. The integrated approach was designed to provide a compelling body of scientific evidence to support Eriodictyol as a viable natural therapeutic candidate for the treatment of breast cancer and in turn provide a foundation for subsequent preclinical and clinical development programmes.

2. Materials and methods

2.1. Dataset collection

The current study used a dataset that was derived from BindingDB, made up of compounds with known binding to the progesterone receptor. Each entry consisted of the monomer identifiers, SMILES (Simplified Molecular Input Line Entry System) strings, and IC_{50} values in nanomolar (nM). For quantitative predictive modeling, IC_{50} values were logarithmically transformed to give pIC_{50} values. Chemical validity checks were performed using RDKit and Open Babel, which are popular chemoinformatics tools to check the structural integrity of the SMILES strings. Molecules with invalid or chemically ambiguous SMILES were removed from downstream analysis. Molecular descriptors were then calculated with the Mordred descriptor calculator, which provides a wide range of structural and physicochemical molecular descriptors for each molecule [20]; [21]. Based on the pIC_{50} values, compounds were classified into three categories: least active ($pIC_{50} \leq 5.0$), moderately active ($5.0 < pIC_{50} \leq 7.5$), and active ($pIC_{50} > 7.5$).

2.2. Data preprocessing and feature selection for machine learning modeling

The resulting descriptor matrix was then processed with a rigorous pre-processing pipeline that was developed to protect the integrity of features and make it suitable for further machine learning steps. Descriptors with missing or null entries were removed to maintain completeness of data. Features with zero variance across the data were removed after a constant-filtering step, and those with very small variance (threshold <0.01) were excluded because of insufficient discriminatory power. Multicollinearity was reduced by omitting descriptors whose Pearson correlation coefficient with any other descriptor was greater than 0.75. Outliers were identified and removed by Z-score of ± 7 thereby enhancing the robustness of the dataset. The descriptors were then ranked by variable importance measures and only those descriptors which were informative for Progesterone receptor bioactivity classification were selected. Finally, the dataset was split into training and testing subsets in a 70:30 ratio, to ensure balanced representation in the development and evaluation of the model [22].

2.3. Model building

Here, we applied a diverse ensemble of machine learning algorithms in the construction of classification models to identify the bioactivity of compounds on the progesterone receptor (PR). The toolbox algorithms included Random Forest, Instance - Based k - Nearest Neighbour (IBK), Multilayer Perceptron, Decision Tree, Logistic Regression, Sequential Minimal Optimization (SMO), K - Star and Naive Bayes. All the models were implemented by means of WEKA software platform, which is a full-scale data mining and supervised classification environment. The performance of models was evaluated based on the accuracy, Cohen K statistic, Mean Absolute Error (MAE), Root Mean Squared error (RMSE), Relative Absolute error (RAE) and Root Relative Squared error (RRSE). In order to enhance robustness and to minimize overfitting, 10-fold cross-validation was applied together with the typical 70:30 training-test split [23]; [24].

2.4. Compound library preparation

In IMPPAT (Indian Medicinal Plants, Phytochemistry and Therapeutics) database, a phytochemical library of 71 compounds was isolated in *Ocimum tenuiflorum* to determine the potential bioactive molecules against progesterone receptor. The chemical structures of these phytoconstituents were highly curated and normalized with chemistry-informatics tools like RDKit and Open Babel, to guarantee the accuracy of the molecular descriptors calculation and the structural

integrity of any given compound. This library of curated compounds was then submitted to predictive modelling with optimized machine-learning classifiers. Compounds were described as active and ranked based on further in silico confirmation of binding affinity, interaction stability and specificity to the progesterone receptor (molecular docking and molecular dynamics simulations).

2.5. Network analysis

The concept of network pharmacology is highly multidimensional in its approach to the study of the relationship between pharmacologic entities and disease mechanisms. In our study we combined the latest network pharmacology methodology with Eriodictyol, as an active compound and the interaction analysis with the network was conducted using STITCH software and Swiss Target Prediction. The computational tools were applied to Eriodictyol as a model drug and the potential targets of the drug, particularly, breast cancer. The targets were selected, filtered, and annotated with DisGeNET to establish the possible therapeutic value of Eriodictyol. The molecules were chemically characterised, functionally and structurally analyzed with ChemDraw, Pymol, and SwissADME. These applications allowed to monitor the most important molecular properties and to investigate potential pharmacological uses of Eriodictyol. Furthermore, the breast-carcinoma-associated protein 3ZR7 (PR) was analyzed using the Cytoscape and STRING to comprehensively characterize its involvement in oncogenic pathways and related processes. The systematic review places emphasis on the potential of Eriodictyol as a potential therapeutic agent for the treatment of cancer due to its capacity to target identified oncogenic pathways [25–27].

2.6. Protein analysis

The conformation of a protein is intimately related to their function and there can be a strong relationship between the structural integrity of proteins and their biological activity. Ramachandran plot generated by PROCHECK program at the European Bioinformatics Institute (EBI) and showed the goodness of the protein structure of 3ZR7 (PR) in this research project. The Ramachandran plot scores computed the steric quality of the protein structure, i.e. the extent of the adopted values of the dihedral angles to have the most ideal range. It supports the detection of a conformational fluctuations and where the values deviate from the conformational stability of the protein. Comparative analyses of G-factors crucial to the overall protein stability and protein functionality were also made. In addition, the bond length and the geometrical distribution of residues were examined to make sure that the protein structure has been preserved. The degree of this critical analysis of the structural stability of the protein forms the basis of the biological activity of the protein and of its possible therapeutical use [28].

2.7. Molecular docking analysis

The potential computational approach is molecular docking that provides a detailed description of the binding interface between ligands and target proteins. The present work has been conducted by using the molecular docking protocol to investigate the interaction of different ligands with 3ZR7 (PR) proteins. The PR is a clinically and therapeutically relevant and 3ZR7 is high-quality PR ligand-binding, with high structural reliability. The protein was selected because it has a high crystallographic resolution of 1.65 Å thus; the atomic positions are accurate and the interaction mapping is reliable. The active site is well-defined and of sound and sound conformational integrity, which makes 3ZR7 an appropriate and strong model of assessing the binding properties of Eriodictyol. To tweak the structure of the protein, water molecules were removed and polar atoms needed to favour the enhanced bonding interactions were introduced. Ligand preparation and box specification (X = 10.76, y = 5.17 and z = 8.41) for docking (included all possible sites of protein binding) were carried out. The activity profile of the protein and ligands were considered in detail and docking simulations were carried out using AutoDock Vina. The purpose of such docking analysis was to confirm the fact that the ligands achieve an optimum binding within the active site of the 3ZR7 protein and thus maintain their therapeutic potential. The computational approach provides valuable insights into ligand specificity for modulation of protein functions and is helping with the design of targeted therapeutic intervention [29–31].

2.8. Molecular dynamics analysis

Molecular dynamics (MD) is a computational approach that analyses what happens during the interaction between proteins and ligands at various physiological conditions over time. In the present work, the dynamical behaviour of the ligand molecules in the complex with 3ZR7 (PR)-protein was studied, based on the system of molecular dynamics, using the molecular dynamics programme named Desmond. The simulation environment were performed using the OPLS-2005 force field within Desmond, employing an orthorhombic TIP3P water model, counter-ion neutralization, and 0.15 M NaCl. The system was equilibrated using NVT and NPT ensembles, followed by a 100-ns production run at 300 K and 1 atm, controlled via the Nose–Hoover thermostat and Martyna–Tobias–Klein barostat. Compositional integrity and dynamics of the complex. were determined by calculating the structural parameters including Root Mean Square Deviation (RMSD) and Root Mean Square Fluctuation (RMSF). These parameters are measures of the stability of the protein-ligand complex and thus an important criterion for its therapeutic potential [32,33].

2.9. ADMET analysis

The state-of-the-art programs are known as ADMETlab 3.0, which can be used to predict the ADMET (Absorption, Distribution, Metabolism, Excretion and Toxicity) characteristics of the small molecules, which give an indication of the nature of the pharmacokinetics. The system is based on machine motivated learning algorithms and databases to examine the most significant features that contain intestinal permeability, blood brain barrier permeability, cytochrome P450 enzyme interactions and potential risky toxicity as well. Scholars have the possibility to place the structure of compounds in various forms (SMILES, InChI, MOL) or draw them themselves in the site. Upon submission of a structure, a detailed profiling of pharmacokinetic/safety profile of the compound is analyzed using ADMETlab 3.0. This is reported as scores and graphs in the form as detailed as could enable the researchers estimate drug-likeness and of safety of their compounds. The instrument is extremely significant to drug discovery as it involves a preliminary determination of the pharmacology of prospective treatment agents [25].

2.10. Density functional theory

Density functional theory (DFT) is a quantum-mechanical method of explaining the electronic structure of molecules which in turn can provide important insight into their stability and reactivity. In this study, first principles density functional theory (DFT) simulation of the electronic structure of stigmasterol was performed and the structural information was obtained from PubChem and the connectivity information was used to construct the initial geometry. Subsequently, the geometry was optimized by Spartan14 and the energies of the highest occupied molecular orbital (HOMO) and lowest unoccupied molecular orbital (LUMO) were calculated by Gaussview 6.0.16; the HOMO-LUMO gap was taken as the main descriptor of the electronic properties of the compounds, especially their reactivity and stability. The calculated results reveal a relatively small HOMO-LUMO gap of stigmasterol, indicating low electronic stability and potential energy

band variation stability, which is helpful not only in estimation of the compound's therapeutic potential, but also in the compound chemistry under various conditions [25–27,32–34].

2.11. Formulation of SLNs-Encapsulated eriodictyol

Extraction of Eriodictyol was carried out augmented in bioactive constituents by the ultrasound-assisted ionisation method. The equipment included a 250 mL jacketed reactor (PCI Analytics Ltd., Mumbai, India) coupled with an ultrasonic water bath with temperature regulation of ± 1.0 °C, 220 V power supply and continuous ultrasonic action of a 20 kHz high intensity ultrasound processor. For the ionisation process a 200 mL suspension of 70% ethanol containing 20 g Eriodictyol (particle size 0.5 mm) was used. Therefore, this method has a high extraction capacity for various supplements, is non-toxic in most cases, and an easy recovery of yields can be achieved, which makes it a better method in the biopharmaceutical industry. The ionized residue was filtered in the Whatman No. 1 filter paper. The resultant filtrate was evaporated to dryness under reduced pressure in a rotary vacuum evaporator (Buchi Rotavapor R-200, Mumbai, India) at 40 °C. Ethanol was removed by lyophilization to give a dry powder and stored in a desiccator until the time of experiment [35].

2.12. Eriodictyol loaded SLNs formulation

Eriodictyol was encapsulated into SLNs by ultrasonic and high-speed mixing. The protocol was initiated by dissolving cetyl palmitate in ether and heating it gently to get a homogenous lipid phase. The obtained lipid mixture was then combined with Eriodictyol solution and stable microemulsion was formed by ultrasonic treatment. Polysorbate-80/sodium deoxycholate preformulation was used to stabilise the formulation and a clear stable suspension was obtained. The SLNs were ultracentrifuged at 10,000 rpm and then isolated and purified. The loading efficiency was determined by well-known drug loading capacity and encapsulation efficiency equations. The given methodology proves the great potential of the SLNs as an effective delivery platform and improves the effectiveness of Eriodictyol in therapy.

2.13. In vitro drug release of SLNs-Encapsulated eriodictyol

Dialysis bag diffusion method was used to investigate in vitro release of Eriodictyol encapsulated in SLNs. In the present study, the Eriodictyol-laden SLNs were placed into dialysis membranes (molecular weight cut off of 3500 Da) and then immersed into release media (acetate buffer, pH 5.1; phosphate buffer, pH 7.4) at 37 °C. Finally, high performance liquid chromatography (HPLC) analysis of Eriodictyol release behavior from the SLNs was carried out with time. This method allowed extensive information with regards to the sustained release kinetics which enabled the characterisation of the drug release profiles and validation of the long-term delivery by the SLNs.

2.14. Kinetics of SLNs-Encapsulated eriodictyol

Zero-order, first-order, Higuchi, Korsmeyer-Peppas and Hixson-Crowell models were applied as kinetic models to study the process of Eriodictyol dissolution from solid lipid nanoparticles (SLNs). These models allow to determine the profile of the drug release, as well as the mechanism of permeation of the agent through the biological barriers by the delivery system. From fitting the release data to these models, the release kinetics were quantified as was the Eriodictyol release rate from the SLNs. Kinetic analysis is very useful in formulation optimization of SLN and in development of sustained release profile for maintenances of therapeutic efficacy of Eriodictyol loaded SLNs to the desired level for a prolonged period of time.

2.15. Stability of SLNs-Encapsulated eriodictyol

The parameters which are physiologically relevant to the development of Eriodictyol-loaded solid lipid nanoparticles (SLNs) were researched. The SLNs were prepared in aqueous NaCl, bovine serum albumin (BSA), acetate, phosphate buffer at 35 °C and pH 5.1 and pH 7.4. Ultraviolet-visible (UV-visible) spectroscopy was used to determine time dependent changes in absorbance (λ_{max}) to characterize the stability of the SLNs. The resultant analysis was informative with regard to the structural integrity of the SLNs and their ability to maintain the integrity of Eriodictyol under physiological conditions under investigation. The results showed that the SLNs keep the integrity of the structure intact to such an extent that the encapsulated Eriodictyol could be retained and stored to be reused in the future.

2.16. LC-MS characterization of SLNs-Encapsulated eriodictyol

Liquid chromatography-mass spectrometry (LC-MS) analysis was used to determine the stability and integrity of Eriodictyol trapped in solid-lipid nanoparticles (SLNs). The active material contained in the SLNs was quantified using this analytical technique with a reasonable precision. The LC-MS analysis showed the encapsulation was successful since there was no degradation or loss of Eriodictyol. The spectral data confirm the stability of the encapsulated drug and the possibility of successful delivery of the drug in the SLNs formulation.

2.17. FTIR characterization of SLNs-Encapsulated eriodictyol

FTIR spectroscopy was used to gain insight into the structure properties and dynamics of Eriodictyol loaded SLNs. Shimadzu IR Tracer-100 spectrophotometer was used to record the IR spectra in the range of scanning wavenumber of 400-4000 cm^{-1}. In the compatibility of formulation, FTIR analysis proved to be an essential information, indicating that the Eriodictyol loaded SLN was molecularly compatible and Eriodictyol structure was not altered during the encapsulation process.

2.18. XRAY characterization of SLNs-Encapsulated eriodictyol

The eriodictyol X-ray diffraction was conducted in powder diffraction system using a Cu Ka source (l = 1.5418 A). Before analysis, the eriodictyol sample was dried in a vacuum oven for 24 h at 60degC to eliminate the water content traces and to avoid interferences due to adsorption of water molecules. The as-prepared dried samples were then ground with an agate mortar and pestle into a fine powder to achieve homogeneous particle-size distribution to minimize the effect of preferred-orientation. About 50-100 mg of the powdered sample were introduced homogeneously into an aluminum sample holder with a back-loading technique which created a flat and homogenous surface without air gaps or over-compaction. The sample mount was carefully inserted in the goniometer of the diffractometer with perfect orientation of the sample with respect to the incoming X-ray beam. The diffractometer was operated at the normal conditions, and the tube voltage and the tube current were 40 kV and 40 mA, respectively. Data were obtained in continuous-scan mode from 2o to −60o with a step size of 0.02o and a counting time of 2 s/step. Scanning rate = $2^{o}/min^{-1}$ was selected to have adequate peak resolution and statistical reliability. Background correction was performed by polynomial fitting, and the peak finding was conducted by using the automated peak-search algorithms with minimum threshold peak intensity of 3% of the maximum peak intensity. Miller indices were calculated by systematic absences and crystallographic computations. Finally, the diffraction pattern was analyzed by means of appropriate crystallographic software for phase identification and structural characterization by comparison of the observed d-spacings with databases based on standard reference data [36].

2.19. FE-SEM analysis of SLNs-Encapsulated eriodictyol

Field Emission Scanning Electron Microscopy (FE-SEM) was used in this study for morphology and size distribution study of Eriodictyol loaded SLNs. Subsequently the freeze-dried SLNs were resuspended in distilled water prior to further characterization. The homogeneity and stability of the SLNs were reinforced by the FE-SEM micrographs showing that they are compatible as drug-carriers and indicating their potential to be used as controlled-delivery drug delivery vehicles.

2.20. Particle size analysis of SLNs-Encapsulated eriodictyol

Solid lipid nanoparticles (SLN) of the bioactive agent eriodictyol were prepared by ultrasonic assisted ionic method and the resulting formulation maintained the bioactive ingredients. The ultrasound-assisted ionisation apparatus was composed of a jacketed reactor (250 mL, PCI Analytics Ltd.) and ultrasonic bath (220 V, +-1.0degC) with continuous operation frequency of 20 kHz. Eriodictyol powder (with a particle size of about 0.5 mm) was suspended in 200 mL of 70 % ethanol; this suspension and methanol were sonicated under the specified ionisation conditions at 0.4 % power. The resulting ion species showed broad material applicability, inherent non-toxicity, and straightforward recovery and therefore would be attractive for biopharmaceutical applications. The plant residues were filtered through Whatman No. 1 filter paper. The filtrate was evaporated in Buchi rotavapor R-200 rotary vacuum evaporator (Mumbai, India) at 40degC. It was subsequently lyophilized to give dry powder. Residual ethanol was evaporated and stored in desiccator for experiment.

2.21. MTT assay

Cell viability of Eriodictyol loaded SLNs in MCF-7 was studied by measuring the minimum inhibitory concentration (MIC) using the Musicin Test Method (MTT assay) after ethanol-induced treatments at various concentration levels (20, 30, 60, 120, 240 and 500 μg mL^{-1}). The MTT assay is the most frequently used method for quantification of cellular metabolism and relies on the conversion of water-soluble yellow tetrazolium salt (MTT) to insoluble dark blue/purple formazan crystals by mitochondrial dehydrogenases of metabolically active cells to provide reliable colorimetric and quantitative measurement. MCF-7 were seeded in a 96-well tissue culture plate at 1×10^5 cells mL^{-1} (100 μL per well) for 24 h at 37 °C. After 24 h, these cells were washed and the growth medium was aspirated. The test samples were cultivated in RPMI medium with 2% serum after serial, two-fold dilutions. Three non-treated wells were incubated with serum alone and the remaining wells with 0.1 mL from each diluted sample. Further incubation was performed at 37 °C and the metabolic status of cells was analyzed. We then added 20 μL of 5 mg mL^{-1} solution of MTT (prepared in PBS) to each well and incubated the plates vigorously for 5 min, then 4 h at 37 °C in 5% CO_2, to allow for the formation of formazan. Formazan crystals were dissolved in the 200 μL DMSO and shaken vigorously at room temperature for 5 min. Absorbance was measured at 560 nm. The experimental protocol was cycled three times. Cell viability was determined by the formula: Cellular viability (%) = At/Ac = 100 where At and Ac are the mean absorbance of Eriodictyol-loaded SLN-treated cells and control cells, respectively (n = 3 independent experiments).

3. Results and discussion

3.1. Comparison of machine learning models

The descriptors were chosen from the comprehensive Mordred set because they capture key physicochemical, topological, electronic, and structural features known to influence ligand–receptor interactions. A rigorous preprocessing pipeline-including variance filtering, correlation reduction, and feature-importance ranking-ensured that only the most informative descriptors relevant to progesterone-receptor bioactivity were retained. The classification accuracy of several machine learning algorithms for the prediction of bioactivity of compounds against the progesterone receptor was assessed using established metrics of accuracy, Cohen's kappa, mean absolute error (MAE), root-mean-square error (RMSE), relative absolute error (RAE), and root relative squared error (RRSE). The best predictive performance was the Random Forest algorithm, with its accuracy of 78.12%, kappa statistic of 0.5361, and the lowest error estimates, with an MAE of 0.2004 and an RMSE of 0.3204, proving to be the most precise predictive model with very low deviation from observed bioactivity measurements. The accuracy of the Decision Tree algorithm was 75.85%, and the kappa was 0.4716 while the accuracy of K-Star and the kappa were 75.19% and 0.4679, respectively. On the other hand, Naive Bayes, Multilayer Perceptron, Logistic Regression and Smo models provided lower accuracies (69.91%, 75.19%, 71.89% and 71.72% respectively), lower kappa values and higher error metrics, indicating relatively lower robustness in the classification. In order to check the generalizability, the obtained Random Forest classifier was further tested on an independent test set, resulting in an accuracy of 79.98%, a kappa of 0.6414, and MAE and RMSE of 0.1825 and 0.3107, respectively. These results confirm the reliability of the model and support the robustness of our approach, and make the Random Forest an effective tool to achieve accurate prediction of biocidal activity at the PR, with significant implications for drug discovery activities Figs. 1–5 and Tables 1–4. The analysis of ROC-AUC in addition to the reported accuracy (78.12%), to estimate the discriminative performance across the activity classes as well as provided confusion matrices to both the training and independent test sets. These measures give us a better understanding of the sensitivity, specificity and misclassification tendencies, which prove the quality of the model used, which is a Random Forest. The values obtained in the ROC-AUC values, as well as the confusion matrices, reflect high class dichotomy and uniform predictive stability, respectively. The combination of these additions provides a more detailed confirmation of the predictive power of the model.

3.2. Prediction of active constituents for Ocimum tenuiflorum constituents

Finally, the optimized Random Forest model was used to screen a phytochemical library of 311 compounds derived from *Ocimum tenuiflorum*, which was used as an assay for possible inhibitors of the Progesterone receptor. Additionally, eight compounds were identified as active according to calculated molecular descriptors, and hence potential therapeutic agents for the Progesterone receptor target. The active constituents identified are: 157-Octatrien-3-ol, 37-Dimethyl-3R5E-E−26-Dimethylocta-57-en-4-one, Geranylacetate, Geranylbutyrate, Alpha-Bergamotene, Thujopsene, Xanthomicrol and Eriodictyol. In order to validate these predictions, further computational studies (molecular docking and molecular dynamics simulation) will be performed to determine the affinity, interaction stability and specificity at the Progesterone receptor active site. The information from these computational assessments will help prioritize the compounds for experimental validation to further develop them as drug candidates.

3.3. Network analysis

Topology analysis of the network implied that the interaction was intricate with the proteins able to display fluctuating centrality values of the network that suggest their dissimilar role in cellular signaling. Progesterone receptor (PR) was the highest degree proteins with 57, MAPK 56, and BRCA1 52 were the second, third best connected, and central regulatory factors of biological processes. TP53, PTEN, and PARP with all a degree of 49 showed a high degree of betweenness centrality (16.63) and closeness (0.0204) meaning that they are the most intermediary controlling and most efficient communicating across the network. This underlines their functions as major signaling

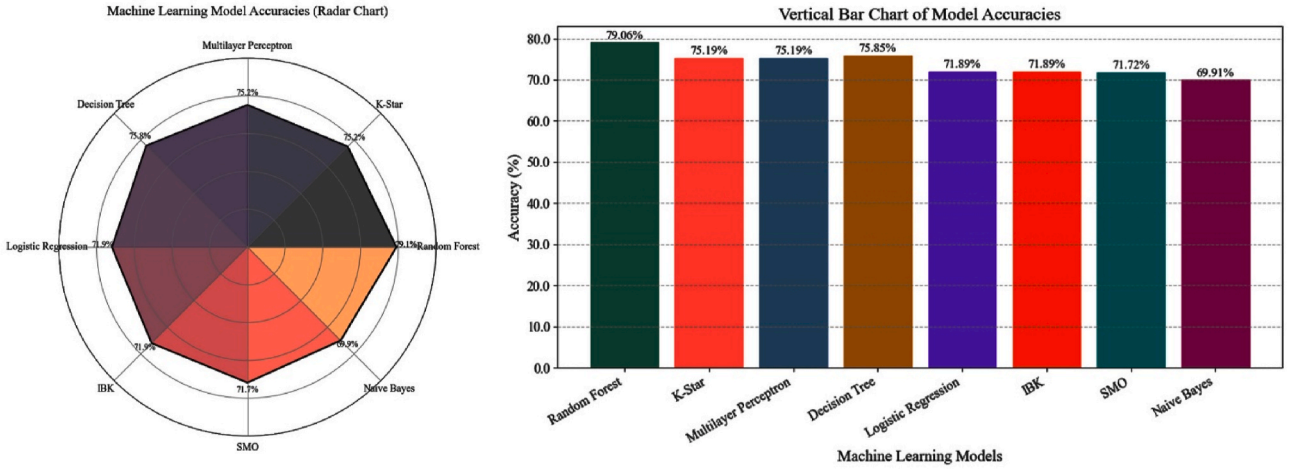

Fig. 1. Comparison of machine learning model performance showing Random Forest achieving highest accuracy (79.06%) among eight algorithms, with radar and bar chart visualizations displaying classification accuracy percentages across different modeling approaches.

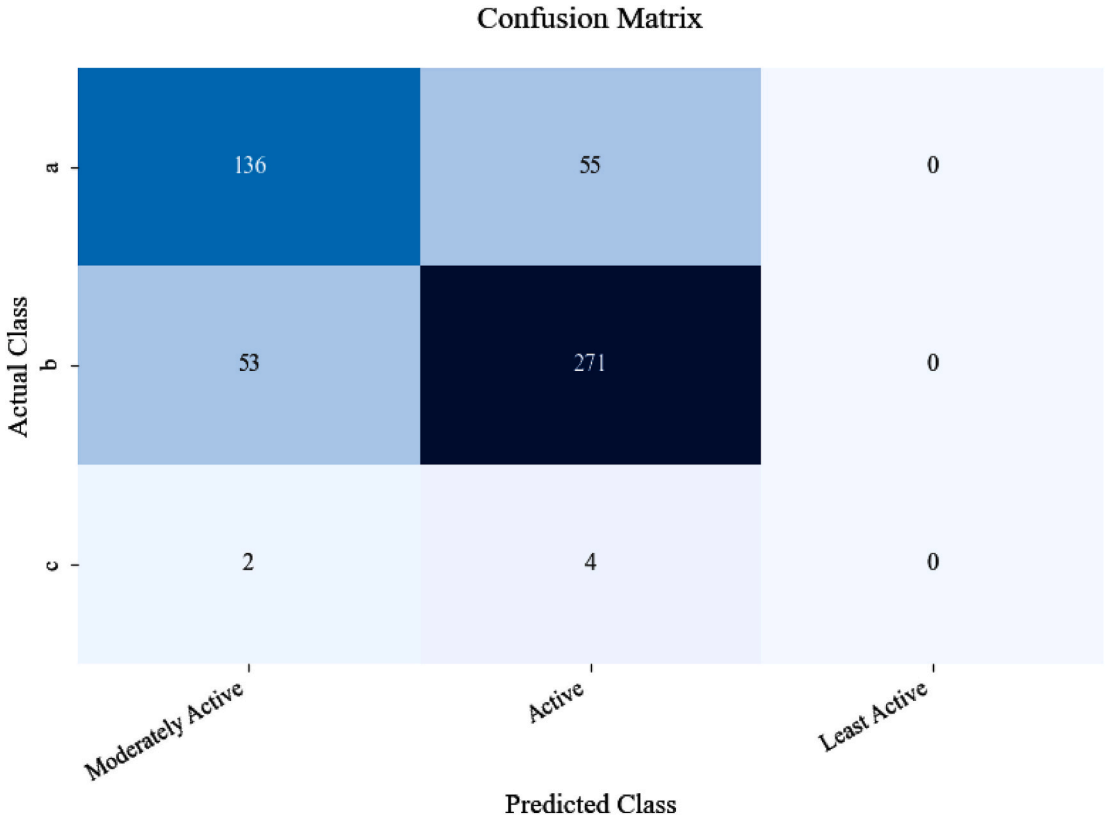

Fig. 2. Confusion matrix displaying classification results for three activity levels, showing strong performance with 136 correctly classified "Moderately Active" and 271 "Active" cases, with minimal misclassifications and no "Least Active" predictions.

intermediates and possible road blocks in oncogenic and stress-response pathways. ERBB2, KRAS, and SMAD4 proteins showed moderate levels (4847) with the same degree of closeness and eigenvector value indicating their moderately influential albeit balanced role in cross-pathway communication. TP53, PTEN and PARP also displayed maximum eccentricity (1) and radiality (2), which is again their core roles in the interactome, and may be an indication of their key role in the repair of DNA, apoptosis and tumor suppression. On the other hand, the BRD4 and BCL2 that had smaller degree and eigenvector scores (0.115 and 0.139, respectively) were more peripheral but seemed to play an important role in transcriptional regulation and anti-apoptotic signalling. Interestingly, the stressed parameter which means carrying potential of the network was highest in TP53, PTEN, and PARP (424), then in KRAS and CDKN2A (390394), as they are more robust and have key-role in signaling cascades. Overall, the network representations suggest that TP53, PTEN and PARP are the regulators of signal transduction integrity, with MAPK and PR serving as cross-linking nodes between the metabolic and hormonal pathways. These combined network measurements are thereby supportive of a hierarchical but collaborative regulation paradigm, and provide a mechanistic guideline on how to rank any therapeutic modulation targets and pathway-based drug discovery objectives. Fig. 6 and Table 5.

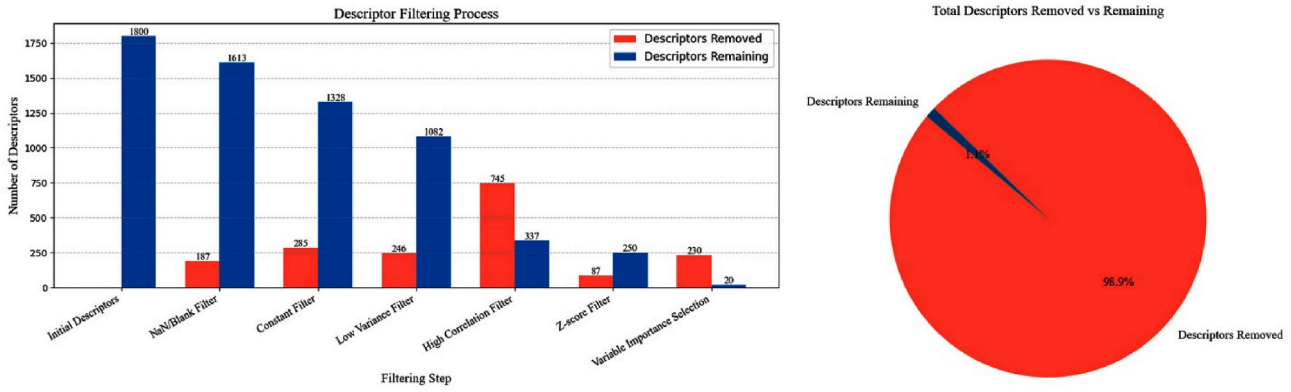

Fig. 3. Feature selection pipeline showing progressive descriptor reduction from 1800 initial features to 36 final features through seven filtering steps, with pie chart illustrating 98.9% of descriptors were removed during the optimization process.

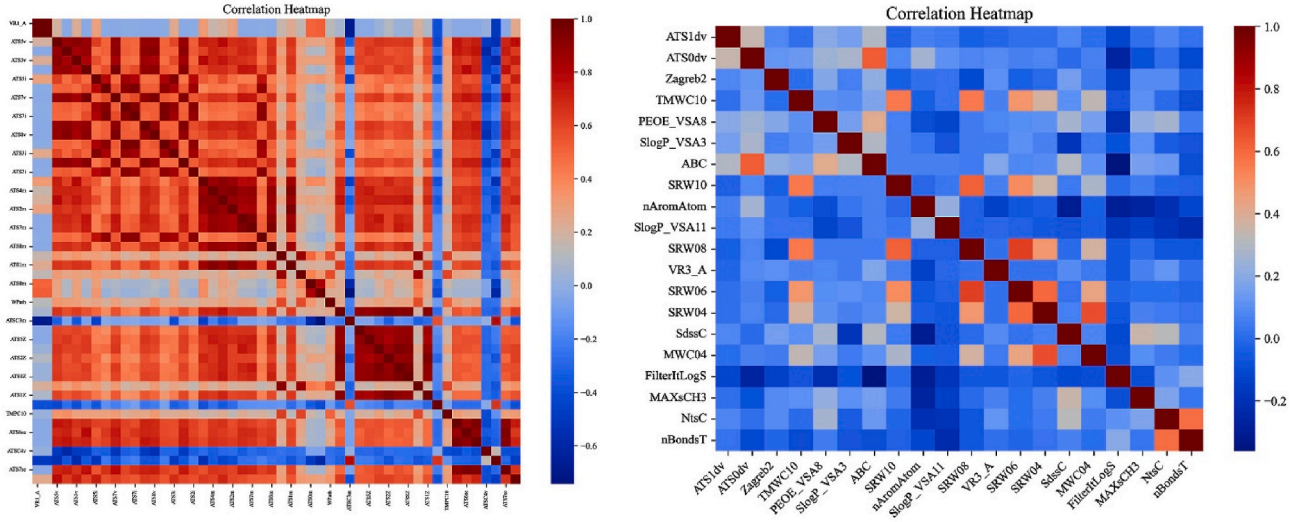

Fig. 4. Correlation heatmaps displaying feature relationships before (left) and after (right) descriptor filtering, showing reduced dimensionality from complex multi-feature correlations to simplified 20-feature matrix with clearer correlation patterns.

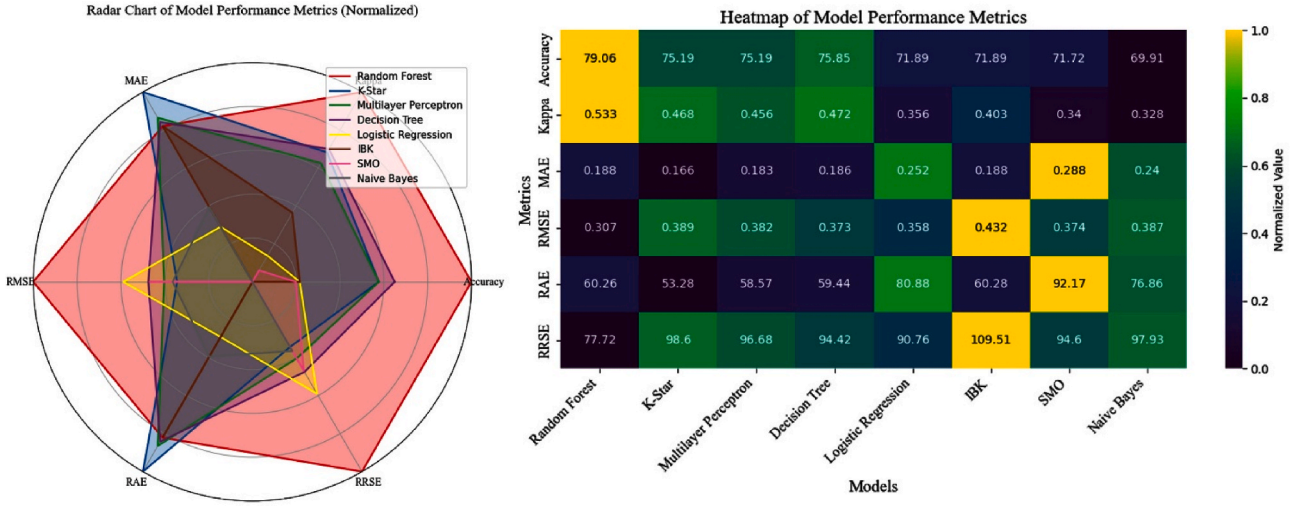

Fig. 5. Comprehensive model evaluation using radar chart and heatmap displaying normalized performance metrics (accuracy, Kappa, MAE, RMSE, RAE, RRSE) across eight machine learning algorithms, with Random Forest demonstrating optimal overall performance.

Table 1
Performance comparison of various machine learning models, including Random Forest, Kstar, Decision Tree, IBK (k-NN), Multi-Layer Perceptron, Naive Bayes, Logistics, and SMO, evaluated using accuracy, Kappa, MAE, RMSE, RAE, and RRS metrics on a test set.

Model	Accuracy (%)	Kappa	MAE	RMSE	RAE (%)	RRS (%)
Random Forest (RF)	76.67	0.6439	0.2348	0.3396	53.67	72.61
Kstar	75.93	0.6319	0.1651	0.3876	37.73	82.87
Decision Tree	72.59	0.5825	0.2022	0.4077	46.22	87.18
IBK (k-NN)	70.74	0.5514	0.1981	0.439	45.28	93.86
Multi-Layer Perceptron	67.04	0.4983	0.2356	0.4414	53.86	94.39
Naive Bayes	65.19	0.4717	0.2631	0.4321	60.15	92.38
Logistics	61.48	0.412	0.2735	0.404	62.51	86.38
SMO	60.37	0.3812	0.3152	0.4084	72.05	87.33
Test set	Accuracy (%)	Kappa	MAE	RMSE	**Total Instances**	
Random forest	70.83	0.5396	0.2483	0.3583	116	

Table 2
A confusion matrix representing the classification of compounds into activity categories (Moderately Active, Active, Least Active), showing the distribution of compounds across these categories based on their activity levels.

	a (Moderately Active)	b (Active)	c (Least Active)
a (Moderately Active)	29	21	0
b (Active)	11	27	0
c (Least Active)	0	3	25

Table 3
Descriptor selection process for a dataset, illustrating the number of descriptors removed and remaining after applying various filters, including NaN/Blank, Constant, Low Variance, High Correlation, Z-score, and Variable Importance.

Filter Step	Descriptors Removed	Descriptors Remaining
Initial Descriptors	-	1800
NaN/Blank Filter	187	1613
Constant Filter	288	1325
Low Variance Filter	225	1100
High Correlation Filter	800	300
Z-score Filter	40	260
Variable Importance	240	20

3.4. Protein analysis

PR is a clinically important hormonal biomarker of breast cancer, and it has a powerful effect on the tumour progression, therapeutic response, and resistance patterns. The PR targets have a mechanistically different set of pathways than either ER or HER2, meaning that other therapeutic strategies can be identified, and thus the rationale to consider Eriodictyol versus this understudied target.

An extensive structural study of 490 protein residues from the structural dataset revealed an excellent conformational quality and stability features. Ramachandran plot validation showed that 97.8% (479 of 490) of the residues reside in the favoured conformational regions, whereas only 2.2% (11 residues) occupy the allowed regions. No residues were located in forbidden or outlier regions, confirming high quality protein structures with minimal geometric strain or unfavourable backbone conformations.

The statistical analysis of the torsion angle distribution showed the normal trends of the backbone flexibility, and the average of the torsion angles ps and phi of −4.7deg and −66.2deg, respectively. The distribution of this kind of structure suggests that the main components of the secondary structure are of a helical and sheet nature, which is typical of globular proteins. The fact that the data in the angle of phi are distributed relatively narrowly, compared to that in the angle of psi, is indicative of well-ordered secondary structures, whereas the broader distribution of the data in the angle of psi is indicative of the conformational heterogeneity required to allow proteins to fold functionally. To obtain the data on the dynamics and crystallographic quality of the structure, temperature factor (B-factor) analysis was conducted. The global B-factor with a mean of 20.12U can be characterised as a moderate degree of structural flexibility, observed in protein structures in physiological conditions, refined to convergence. The B-factor scale is between 9.2 and 60.0 U and indicates the non-homogeneous distributions of mobility among protein regions where a low B-factor value is associated with a rigid structural core and a high B-factor value is associated with a flexible surface loop or domain interface. The structural integrity and the crystallographic quality of the dataset are further confirmed by the absence of disordered annotations of any residues. Collectively, these findings indicate that the protein structures being studied are of superior quality and can be used to conduct informative structural-functional relationship studies, and the good geometric validation parameters can be used to perform downstream computational analyses and structure-based drug design studies reliably Fig. 7.

Table 4
List of constituents predicted as "Active" based on their chemical structures, including Strychnine, beta-Sitosterol, Rubiprasin A and B, Lucidinprimeveroside, and various complex organic compounds with bioactive potential.

Constituent	Predicted Class
Strychnine	Active
beta-Sitosterol	Active
(1R,4S,7S,10S,13R,16R)-24-hydroxy-10-[(4-methoxyphenyl) methyl]-4,7,9,13,15,29-hexamethyl-22-oxa-3,6,9,12,15,29-hexazatetracyclo[14.12.2.218,21.123,27]tritriaconta-18,20,23,25,27(31),32-hexaene-2,5,8,11,14,30-hexone	Active
(1R,2R,4aS,6aR,6aS,6bR,8aR,10S,12aR,14bS)-10-hydroxy-2-(hydroxymethyl)-1,6a,6b,9,9,12a-hexamethyl-2,3,4,5,6,6a,7,8,8a,10,11,12,13,14b-tetradecahydro-1H-picene-4a-carboxylic acid	Active
(1R,2R,4aS,6aR,6aS,6bR,8aR,10S,12aR,14bS)-2-(hydroxymethyl)-10-[(E)-3-(4-hydroxyphenyl)prop-2-enoyl]oxy-1,6a,6b,9,9,12a-hexamethyl-2,3,4,5,6,6a,7,8,8a,10,11,12,13,14b-tetradecahydro-1H-picene-4a-carboxylic acid	Active
Rubiprasin A	Active
Rubiprasin B	Active
(1R,2R,4aS,6aR,6aS,6bR,8aR,10S,12aR,14bS)-10-hydroxy-2-(hydroxymethyl)-1,6a,6b,9,9,12a-hexamethyl-2,3,4,5,6,6a,7,8,8a,10,11,12,13,14b-tetradecahydro-1H-picene-4a-carboxylic acid	Active
Ruberythric acid	Active
Lucidinprimeveroside	Active

3.5. Mechanism of action

Progesterone receptor (PR) is a nuclear hormone receptor which is considered as a key biomarker in the classification and selection of treatment of breast cancer. The PR-positive tumor which is about 70 percent of breast tumor in combination with ER-positive status reflect the presence of the hormone receptor-positive disease which has a good prognosis. Mechanism of action Progesterone attaches to PR, and the resulting complex is translocated to the nucleus bringing about gene transcription to stimulate cell proliferation. This pathway is endocrinologically targeted during treatment. Tamoxifen inhibits estrogen receptors, which indirectly inhibits PR expression. Aromatase inhibitors (letrozole, anastrozole) lower the level of estrogen synthesis which limits the activation of the ER and PR pathway. Fulvestrant completely degenerates estrogen receptors. The PR-positive status is predictive of improved response to these hormonal therapies that lower the risk of recurrence by 40-50 percent Fig. 8. Therapeutic decisions regarding individual therapy in the management of hormone receptor-positive breast cancer are very important as treatment frequently lasts 5-10 years.

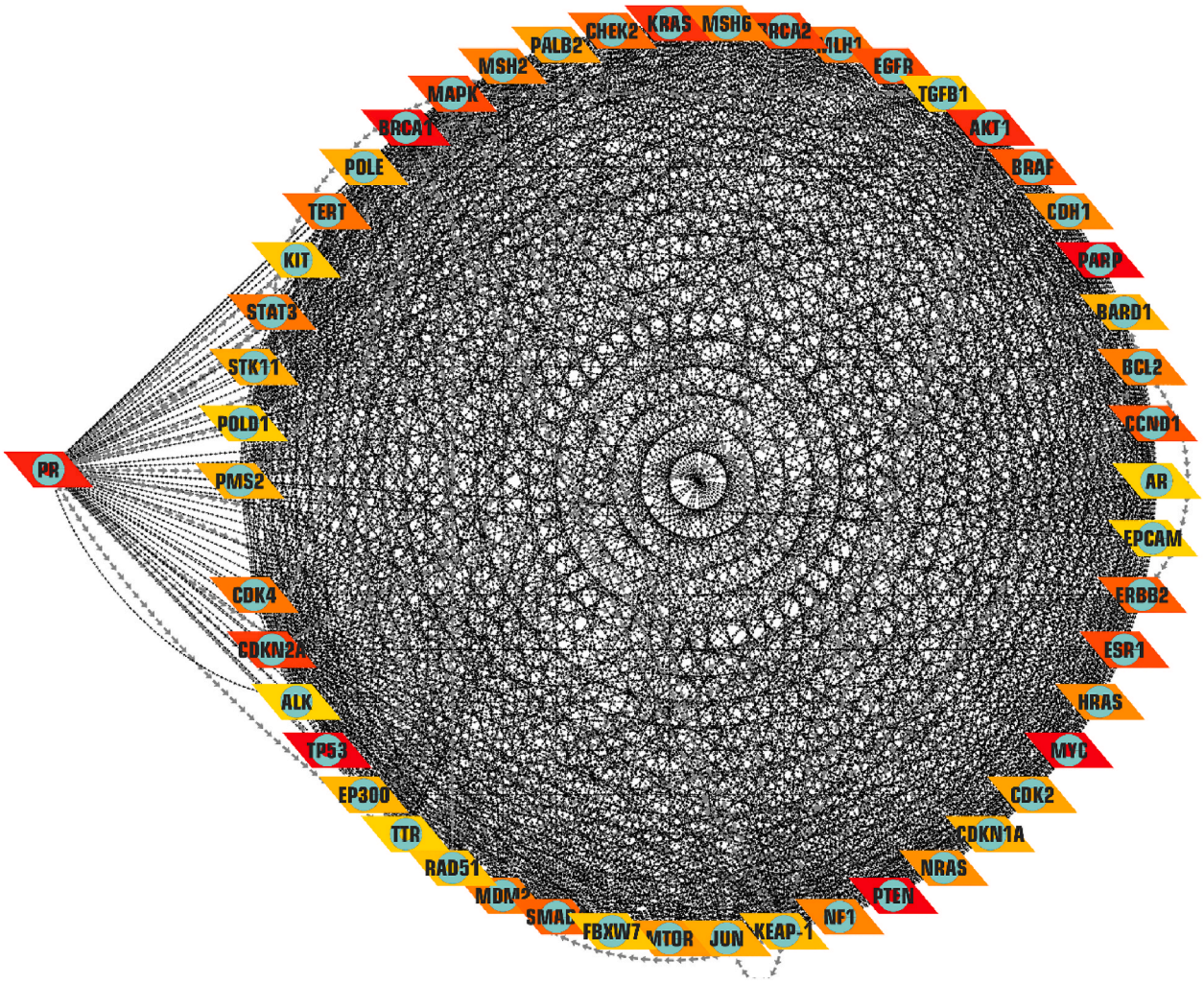

Fig. 6. Protein-protein interaction network visualization displaying comprehensive molecular interactions with gene symbols positioned around the periphery, connected by lines representing functional associations and regulatory relationships between proteins.

3.6. Molecular docking

Docking of 323 natural constituents to 3ZR7 protein target revealed a broad range of binding affinities of 3ZR7, that is, −14.4 to +9.6 kcal mol-1. The highest affinity ligands were Eriodictyol (−14.4 kcalmol-1), Kaempferol (−12.0 kcalmol-1) and Quercetin (−11.6 kcalmol-1), all flavonoids. The three polyphenolic compounds in this article exhibited significantly more interactions than the rest of the library, implying that they are good lead compounds to be used in drug discovery. The most common of the strongest binders were flavonoids, meaning that molecules with multiple phenolic hydroxyl groups in the binding pocket were preferred.

The secondary level was composed of 85 compounds having binding scores of −8.0 to −7.0 kcal/mol. This fraction was composed of various classes of chemicals including sesquiterpenes (a-Cadinene, b-Cedrene, g-Gurjunene), phenolic acids (Rosmarinic acid) and glycosides (Esculin). The fact that terpenoid structures dominate this affinity window implies that they have favourable hydrophobic interactions with the protein binding pocket. Notably, the strongest non-flavonoid ligand was the Rosmarinic acid (−9.8 kJ mol-1), which proves the relevance of the carboxylic acid moieties in the receptor affinity.

The docking scores were distributed in a clear structure-activity relationship: ligands with aromatic ring systems and hydrogen-bond acceptors/donors were more likely to be affine. Monoterpenes and low-molecular-weight entities, in contrast, tended to be less strongly binding with a score of −4.0 to −6.0 kJ mol-1. Three of the compounds showed negative docking scores, i.e. b-Carotene (−1.1 kcal mol-1) and S-2-(3,4-dihydroxyphenyl)-7-(b-D-glucopyranosyloxy)-2,3-dihydro-5-hydroxy-4H-1-benzopyran-4-one (1.0 kcal mol-1) and Vicenin-2 (9.6 kcal mol-1), indicating undesired interactions. These massive and highly glycosylated structures were likely sterically colliding with the binding cavity, reflecting the size constraints that define successful ligand recognition.

The protein-ligand complex mapping revealed a specific binding pattern with hydrophobic contacts, hydrogen bonds and p-stacked interactions. Three interesting hydrophobic interactions were identified: LEU763A interacts with 2486 and 2487 ligand atoms at 3.56A and 3.80A respectively and TYR890A hydrophobically contacts 2477 at 3.53A. Such interactions are indicative of a stable hydrophobic pocket which can accommodate the nonpolar heads of the ligand.

It was identified that the hydrogen-bonding network was rather complex and had six interactions which were essential in giving the complexity which holds the complex together. GLN725A was one of the most important amino acids to have two hydrogen bonds with 2490 and 397 ligand atoms at a distance of 2.25 A. Donor angles of 130.51° and 140.83° were the best preferred donor angles. MET759A and ARG766A formed one hydrogen bond at 2.88 A and 2.04 A, respectively, but, LEU887A formed one hydrogen bond at 2.26 A. The presence of many amino-acid side chains-polar, charged, and hydrophobic-in the hydrogen-bonding network underscores the versatility of the binding

Table 5
Network analysis of key cancer-related proteins, highlighting their degree, betweenness, closeness, eccentricity, eigenvector centrality, radiality, and stress values.

Protein	Degree	Betweenness	Closeness	Eccentricity	EigenVector	Radiality	Stress
PR	57	13.73322455	0.019608	0.5	0.160728	1.959184	354
MAPK	56	15.22890316	0.02	0.5	0.163266	1.979592	390
BRCA1	52	14.77827892	0.02	0.5	0.163309	1.979592	386
KEAP-1	51	11.2954225	0.018519	0.5	0.150854	1.897959	296
TP53	49	16.63513392	0.020408	1	0.165839	2	424
PTEN	49	16.63513392	0.020408	1	0.165839	2	424
PARP	49	16.63513392	0.020408	1	0.165839	2	424
CDKN2A	49	15.22890316	0.02	0.5	0.163266	1.979592	390
ERBB2	48	12.87537956	0.019231	0.5	0.157375	1.938776	338
KRAS	48	15.50591146	0.02	0.5	0.163117	1.979592	394
SMAD4	47	14.01023285	0.019608	0.5	0.160579	1.959184	358
TERT	46	12.00582917	0.018868	0.5	0.154393	1.918367	316
CDK4	46	13.39930332	0.018868	0.5	0.153385	1.918367	336
BRCA2	46	12.02778539	0.018868	0.5	0.153865	1.918367	318
BRAF	45	11.34765059	0.018519	0.5	0.151577	1.897959	286
MYC	45	10.26241618	0.018868	0.5	0.155801	1.918367	280
BRD4	45	7.33182154	0.015625	0.5	0.115028	1.693878	190
ESR1	45	10.44784613	0.018868	0.5	0.155595	1.918367	284
NRAS	44	7.871036696	0.018182	0.5	0.150391	1.877551	224
CCND1	44	8.429123121	0.018519	0.5	0.153277	1.897959	242
BCL2	44	6.371750066	0.017241	0.5	0.139947	1.816327	178
MSH2	44	9.360373608	0.017857	0.5	0.144505	1.857143	250
EGFR	43	8.839499977	0.017857	0.5	0.145627	1.857143	238
MDM2	43	7.071266387	0.017544	0.5	0.14369	1.836735	194
STK11	43	9.722441271	0.017857	0.5	0.145108	1.857143	254
AKT1	43	8.296583532	0.018182	0.5	0.150007	1.877551	230
NF1	42	7.120236589	0.017241	0.5	0.13977	1.816327	196
CDK2	41	9.7046532	0.017241	0.5	0.137366	1.816327	244
MLH1	41	7.802155011	0.017241	0.5	0.137932	1.816327	212
JUN	40	4.713247735	0.016667	0.5	0.133922	1.77551	136
CDH1	40	3.963355269	0.016949	0.5	0.138339	1.795918	122
CDKN1A	40	5.261294819	0.016949	0.5	0.137546	1.795918	150
STAT3	40	4.469942091	0.016949	0.5	0.137695	1.795918	136
HEK2	40	8.2226045	0.016949	0.5	0.134406	1.795918	218

site with regard to the chemical functionality Fig. 9.

A strong p-stacking interaction was observed between the probe PHE778A and the ligand with a centroid-centered distance of 4.99 Å and stacking angle of 85.81deg. The parallel-displaced p-p interaction with an offset of 0.71 A is energetically favourable and contributes greatly to the increase of the binding stability. A T-type conformation is adopted involving six ligand atoms (2482-2487), suggesting an extended aromatic scaffold that maximises p-electron overlap. The combination of hydrophobic interaction, multiple hydrogen bonding and stacking interaction is a complex binding mechanism ensuring high affinity ligand recognition and stable formation of complex, which is in agreement with the high binding affinity observed in the docking study.

3.7. Molecular dynamics

The stability and flexibility characteristics presented over the 100-ns trajectory were well resolved using molecular dynamics simulation analysis. The protein root-mean-square deviation (RMSD) was greater than 1.0-1.6 Å over the entire simulation time, indicating outstanding structural stability. Rapid equilibration was observed for the first 10 ns, followed by a stable protein backbone conformation with small fluctuations of ~1.2-1.4 Å. The low RMSD profile indicates that the native fold of the protein-ligand complex was maintained irrespective of significant conformational slip, suggesting thermodynamic stability at physiological conditions. In contrast, the ligand was very mobile with RMSD values between 0.2 and 1.8 Å. For the first 20 ns the ligand explored the binding site, followed by relative stability punctuated by conformational sampling. Pronounced excursions to 1.6-1.8 Å were observed at approximately 25, 45 and 80 ns, reflecting transient conformational rearrangements in the binding pocket. These oscillations suggest that, though the ligand is bound, there is enough flexibility to maximize intermolecular interactions and to explore alternate binding modes Fig. 10.

Root-mean-square fluctuation (RMSF) analysis revealed heterogeneous pattern of flexibility distributed over the protein structure. Most residues were moderately flexible, exhibiting RMSF values less than 1.0 Å, which is typical of secondary structure elements. However, several peaks were distinct, with the highest peaks at residues 25, 45, 75, 125, 150 and 200 with values of 1.5-2.1 Å. These high mobility regions are probably ascribed to loops, domain interfaces, or allosteric sites that are conformationally changed upon ligand binding. The central peaks near residues 150-175, however, may be functionally important domains for protein dynamics. Overall, the RMSF profile reveals that ligand binding causes local conformational changes while maintaining global protein architecture, thus supporting the observed binding stability and offering insights to possible allosteric mechanisms.

Hydrogen bond analysis showed temporal variations of contact formation and stability, which indicated dynamic binding interaction in the 100-ns simulation. The absolute number of hydrogen bonds ranged from three to nine contacts per frame, and averaged about five to six hydrogen bonds were retained for the duration of the trajectory. A main chain-hydrogen bond network was observed during the initial equilibration stages within the first 10 ns, succeeded by dynamic sampling with periodic formation and rupture of secondary contacts and, occupancy percentages of the major interacting residues (LEU715, LEU718, GLN725, MET756, and MET759). Increased hydrogen bonding lifetimes were detected at 25, 50, and 75 ns, which correlated with ligand conformational changes detected in the RMSD analysis.

The heterogeneous contribution to binding in the binding network was demonstrated by analysing the residue specific occupancy of the hydrogen bonds. LEU715 and LEU718 were the most occupied at approximately 0.90 and 0.85, respectively, and are symbols of continuous contact formation in the simulation. Most likely these leucine residues are involved in backbone hoop hydrogen bonding or indirect

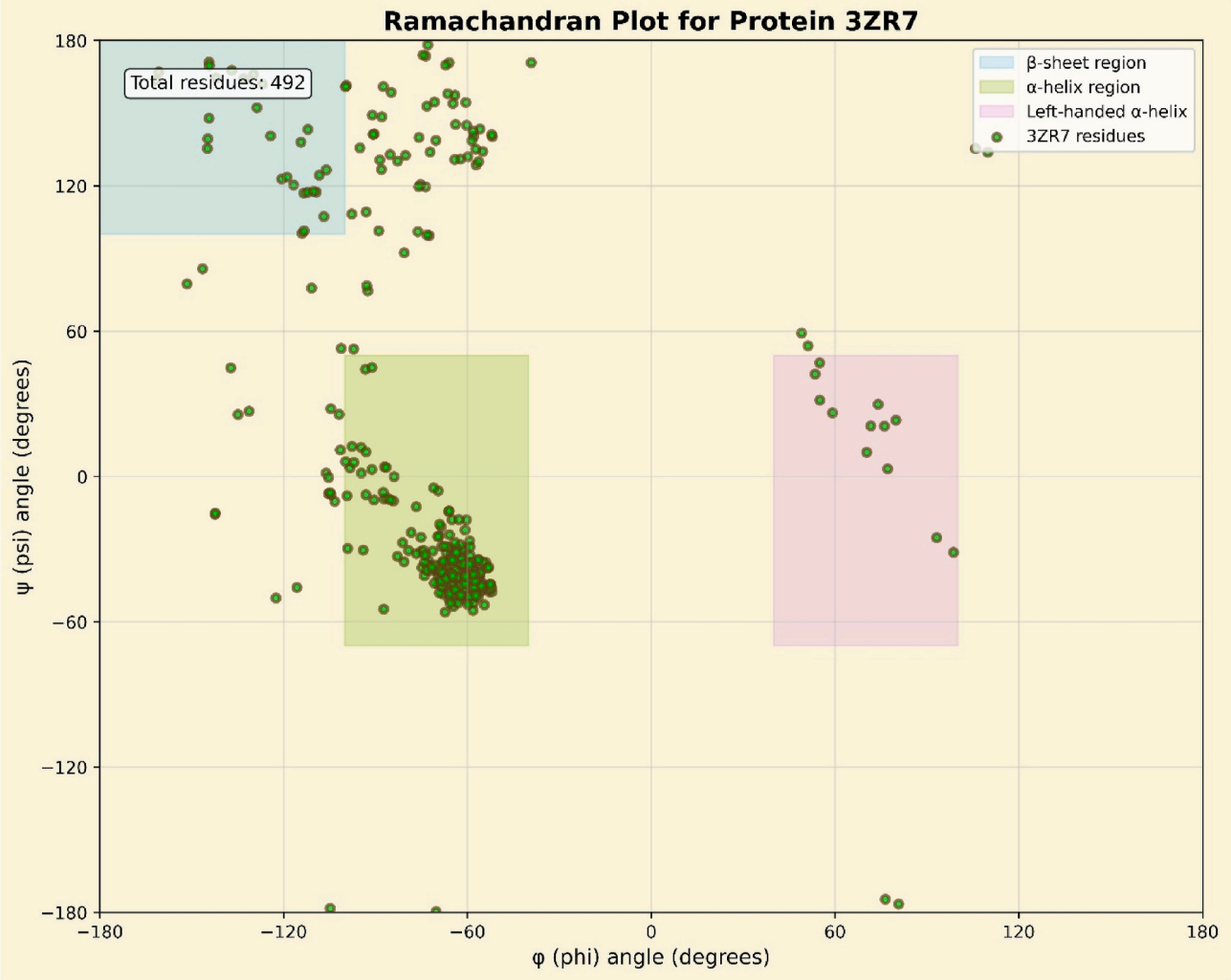

Fig. 7. Ramachandran plot displaying backbone dihedral angles (φ, ψ) for all 492 residues of the protein structure 3ZR7. Colored regions indicate favourable conformations: β-sheet (blue), α-helix (green), and left-handed α-helix (pink).

interaction with water. At the 0.25 position (transient, but possibly functionally relevant contacts) moderate occupancy (ASN719) was observed. GLN725, MET756 and MET759 occupied between 0.5 and 0.8, which is in line with their critical functions based on the analysis of the static binding and contributes to their essential functions to stabilise protein ligand interaction. On the other hand, LEU763, PHE766 and LEU887 were characterised by a low occupancy (0.1-0.3) that might be due to transitory contact formation related to conformational sampling or other binding modes. The PHE778, PHE794 and PHE801 aromatic residues showed low hydrogen-bonding hydrophobically, in keeping with an initial geometry of p stacking between polar contacts. The temporal hydrogen-bonding pattern thereby indicates a dynamic binding model in which core contacts are fixed, peripheral contacts are continuously sampled and binding affinity is optimized under multiple complementary interaction modes to maintain the observed stability, but with enough flexibility to be optimized by induced-fit.

The conformational analysis of the ligand has shown that there is great rotational flexibility around most of the torsional angles during the simulation providing an indication about the binding mode and molecular flexibility. Selective conformational preferences were observed in torsional angle distributions and the characteristic sampling patterns of each of the monitored dihedrals. The torsion angle (blue colour) showed wide distribution between -90^{o} to 0^{o}, with big populations between -180^{o} to $+90^{o}$, suggesting that the ligand was highly rotatable in the binding pocket to assume diverse conformational states. The green and red torsional angles were more limited in their sampling; the green angle was bimodal with modes at −120deg and +60deg and the red angle skewed toward angles between −60deg and +60deg. Such constraints indicate that some of the accessible conformational space of such bonds is restricted due to either the interference with intermolecular interaction or steric hindrance. The orange torsional angle showed a population spread over an intermediate range, with the majority of the population centered around 0^{o} and $+90^{o}$ and lower populations to the extreme -180^{o} indicating a partial restrictive constraint by the binding site. The torsional angle of the purple colour was the least distributed and was centered at -90^{o} to 0^{o}. The conformational preferences inferred are correlated with the chemical structure of the flavonoid ligand and with hydroxyl groups on the aromatic rings being capable of adopting some patterns of hydrogen-bonding which stabilise some conformations. Several hydroxyl substituents provide intramolecular hydrogen bonds and protein-ligand specific interactions and thereby favour preferred torsional states. This conformational experiment indicates that the ligand tends to be binding stable and sufficiently flexible to allow optimization of intermolecular interactions by dynamic conformational sampling, resulting in high binding affinity and facilitating the induced-fit binding mechanism as observed in the simulation trajectory. The comparison of cocrystal and Eriodictyol demonstrated excellent alignment, yielding a RMSD value of 1.42 Å, which is well within the accepted threshold (<2.0 Å) for reliable docking reproducibility. This RMSD confirms that the docking parameters, grid placement, and ligand

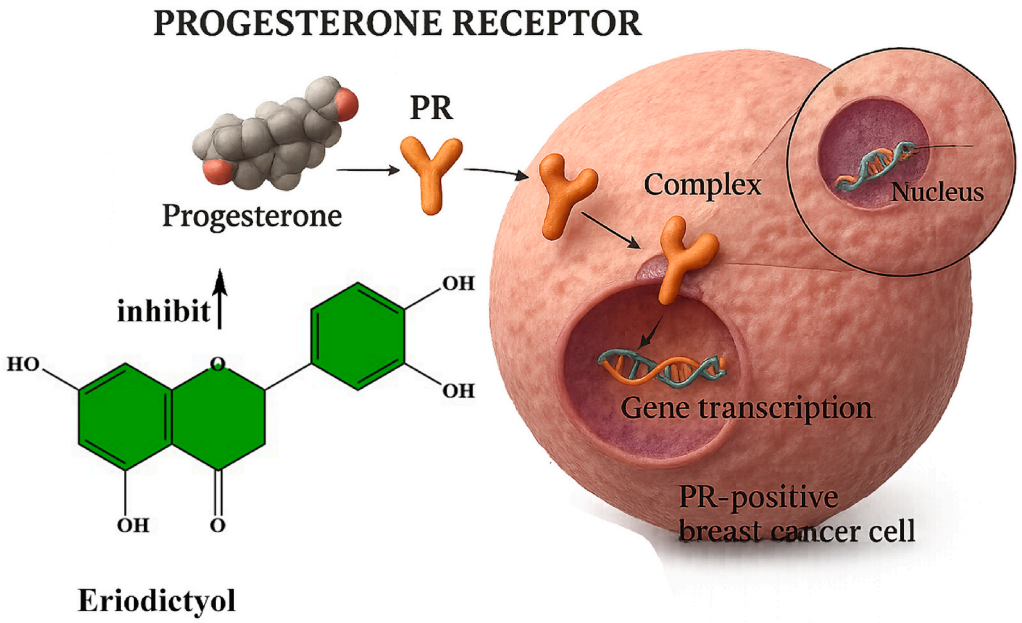

Fig. 8. Illustration showing progesterone binding to its receptor (PR) in PR-positive breast cancer cells, initiating gene transcription, while Eriodictyol inhibits progesterone–PR complex formation, thereby reducing downstream gene expression and tumor proliferation.

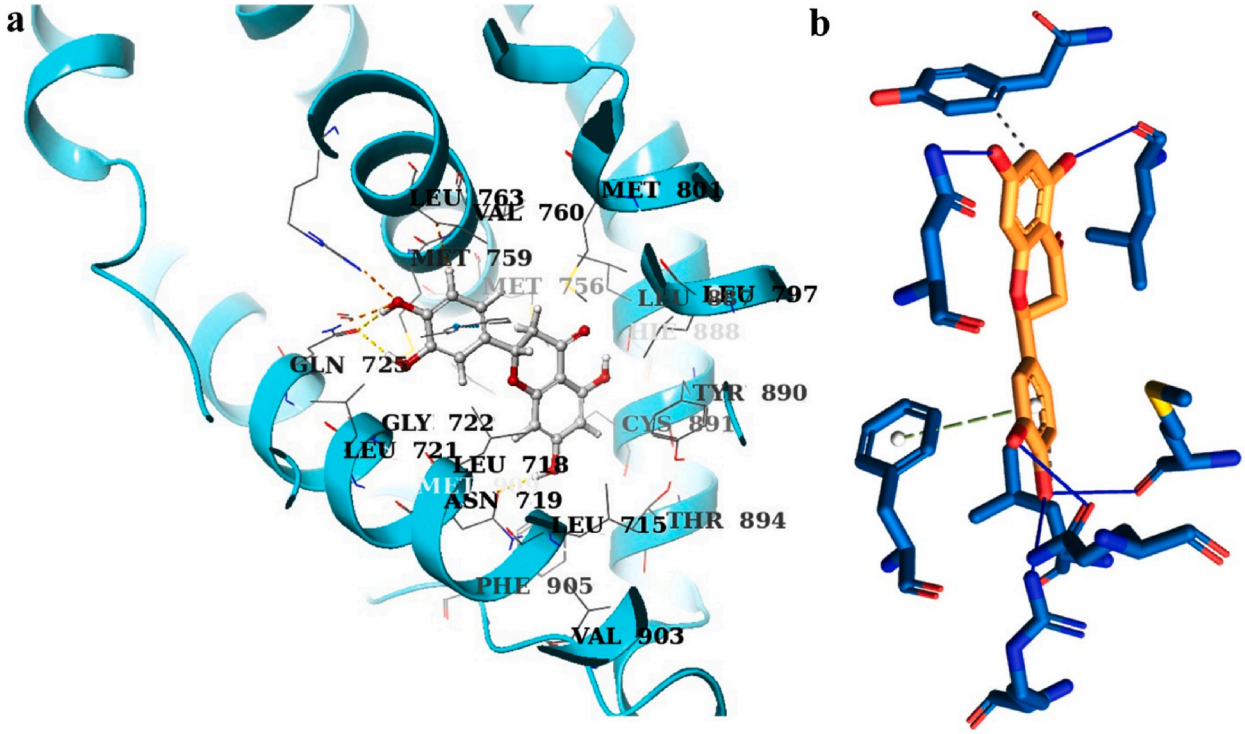

Fig. 9. Molecular docking visualization showing (a) protein-ligand binding site with labelled amino acid residues and interaction distances, and (b) detailed view of binding pocket highlighting hydrogen bonds and molecular interactions between ligand and receptor.

preparation steps accurately reproduce the native binding pose, thereby validating the robustness and reliability of our docking workflow.

3.8. MMGBSA analysis

The energy decomposition analysis of Eriodictyol reveals important insight into the molecular binding mechanisms which describe its biological activity. The total binding free energy (DG) of −51.00kcalmol^{-1} represents strong thermodynamically favourable interactions.

The largest favourable contribution from van der Waals interactions is −67.1 kcal mol^{-1}, confirming a major role for hydrophobic contacts and shape complementarity in Eriodictyol binding affinity. This large contribution demonstrates the significance of the aromatic ring system and the presence of the hydroxyl substituents in creating optimal molecular interactions in the binding site Fig. 11.

Electrostatic interactions are another major favourable contribution

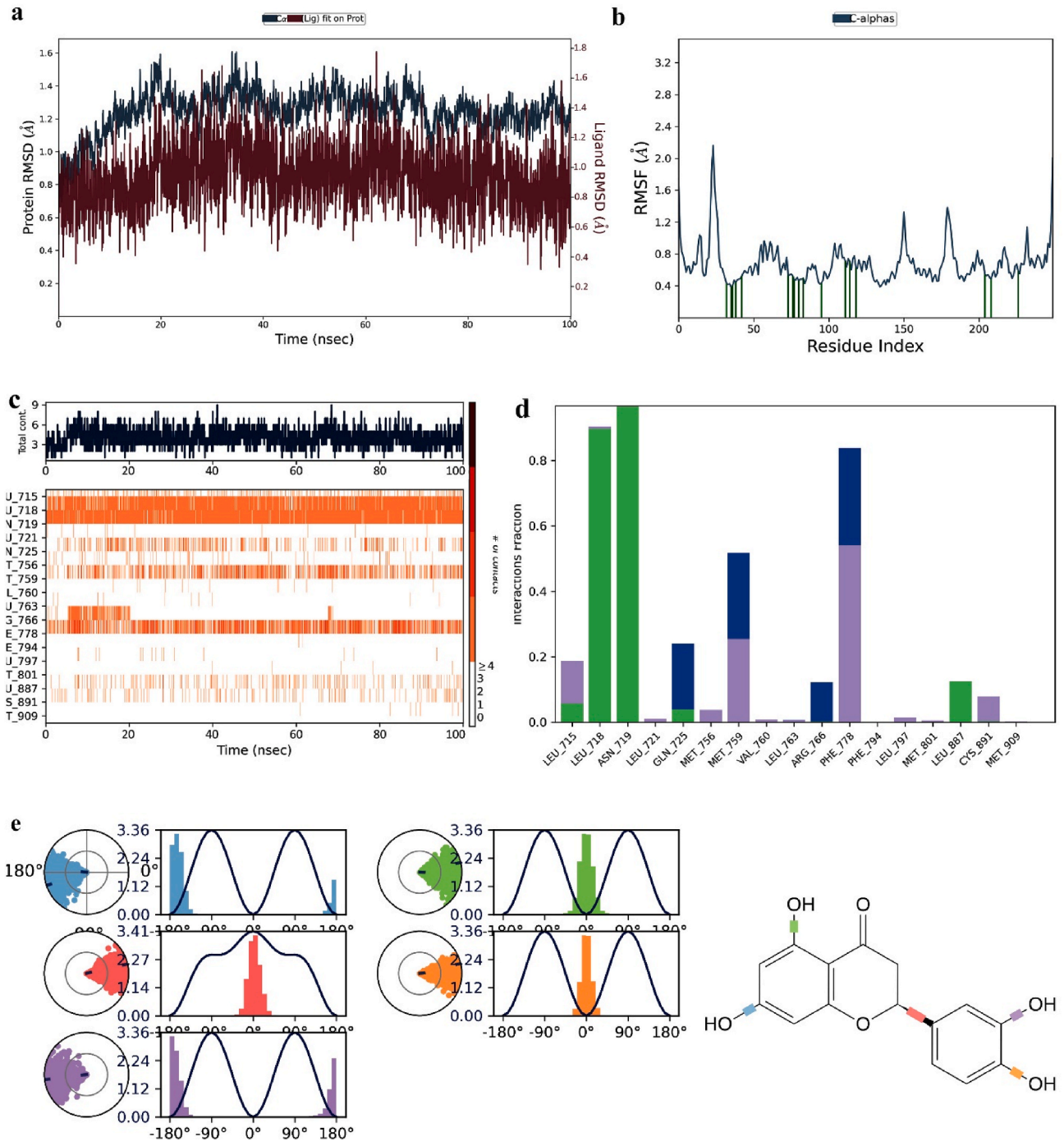

Fig. 10. Molecular dynamics simulation analysis showing (a) protein RMSD and ligand fit trajectories over time, (b) per-residue RMSF fluctuations, (c) ligand contact patterns with binding site residues, (d) interaction fraction analysis, and (e) dihedral angle distributions with molecular structure diagram.

of −42.2 kcalmol^{-1} showing the essential role of hydrogen bonding and ionic interactions. The several hydroxyl groups typical of the flavonoid structure of Eriodictyol probably establish extensive hydrogen-bond networks with polar residues, increasing binding specificity and affinity. The sum of the favourable van der Waals and electrostatic contributions (−109.3 kcal mol^{-1}) is sufficiently large to overcome the unfavourable polar solvation penalty.

Polar solvation contributes the largest energetic barrier (40.1 kcal mol^{-1}), corresponding to the desolvation energy penalty that results when a polar group is buried on binding. This unfavourable contribution reflects the energetic penalty associated with water molecule removal from the ligand as well as polar groups at the binding site. Nevertheless, this penalty is offset by non-polar solvation effects favouring the burial of hydrophobic surface area to a degree of −17.2 kcal mol^{-1} due to the released energy of structured water molecules.

The energy-decomposition profile reveals that Eriodictyol achieves high binding affinity by a balanced combination of specific molecular interactions in which van der Waals and electrostatic forces overcome solvation penalties. This analysis provides important mechanistic insight for structure-based drug design and optimization of Eriodictyol derivatives with improved potency.

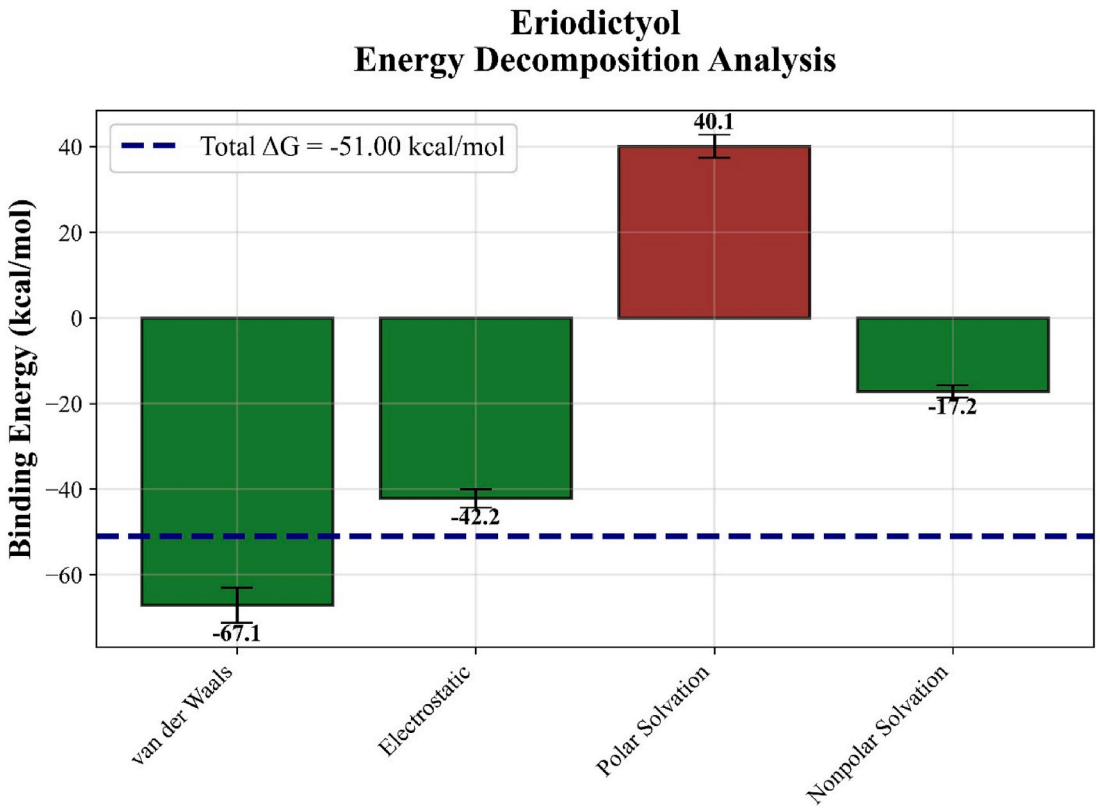

Fig. 11. Energy decomposition analysis of Eriodictyol binding showing individual contributions from van der Waals, electrostatic, polar solvation, and nonpolar solvation components to the total binding free energy (ΔG = −51.00 kcal/mol).

3.9. ADMET analysis

An evaluation of the molecular properties reveals that Eriodictyol possesses desirable drug-like characteristics in various pharmacokinetic and physicochemical properties. The radar plot analysis demonstrates that the properties of the compound fall primarily within the acceptable ranges that are defined by well-known drug-likeness criteria, which provide evidence of a high therapeutic development and oral bioavailability potential.

The MW of Eriodictyol is not far out of the optimum range, meaning that the size is not too large to provide good membrane permeability without being too bulky and risking losing binding affinity through unreasonable entropy penalty. nRot is not far out of the normal range, suggesting that the conformational flexibility is sufficient to accommodate the target without excessively high penalty in entropy. Likewise, the topological polar surface area (TPSA) represents a perfect trade-off, providing the polarity required to be soluble and the lipophilicity required to penetrate membranes Fig. 12.

Within the Rule of Five of Lipinski, both hydrogen bond donors (nHD) and acceptors (nHA) are highly druglike. This favourable hydrogen bonding pattern means a compound will be able to form the required interactions with biological targets and retain the necessary pharmacokinetic characteristics. The number of heteroatoms in the scaffold (nHet), and the ring structure (nRing, MaxRing) of the scaffold, reflect structural complexity that is not too complex to allow target affinity and not too rigid to allow folding.

The values of the partition coefficient (logP) and distribution coefficient (logD) represent an optimal balance of lipophilicity, both of which are of importance in membrane permeability and in tissue distribution. The aqueous solubility (logS) parameter gives us information that has adequate dissolution properties of the development of the formulation and bioavailability. In addition, the formal charge (fChar) and the rigidity (nRig) values verify the drug-like nature of the compound.

On the whole, Eriodictyol exhibits a wide spectrum of molecular property profile which is in good compliance with the standard drug-likeness criteria and therefore is likely to exhibit good absorption, distribution, metabolism, and excretion (ADMET) properties. The properties allow the compound to be considered as a successful pharmaceutical development candidate and it will be a candidate of further preclinical assessment and optimization research.

3.10. DFT analysis

Molecular orbital analysis of Eriodictyol is performed to provide a valuable understanding of the electronic nature and chemical reactivity profile of the molecule. The energy of the highest occupied molecular orbital (HOMO) is −0.32225 eV and that of the lowest unoccupied molecular orbital (LUMO) is −0.19778 eV, HOMO-LUMO energy gap (DE) = 3.387 eV. The high band gap effectively indicates that it is highly electrically stable and mediumly reactive to chemical reactions, and the electronic parameters of Eriodictyol are telling us that it has an intermediate electronic property that is favourable to the biological interactions.

The outcomes reveal a very high localization of HOMO electron density around the site of hydroxylated aromatic ring system, specifically around the phenolic oxygen atom and the adjacent carbon centres. Such a distribution profile suggests these areas to be the most common sites of electron-donation, and to be highly nucleophilic and capable of hydrogen bonding with biological targets. Electron donor sites exist in the hydroxyl substituent aromatic ring systems of Eriodictyol and can easily donate electrons to attack the free radicals and give Eriodictyol antioxidant property Fig. 13.

Conversely, the LUMO electron density is distributed in various patterns along the flavonoid scaffold and is concentrated in the heterocyclic ring system as well as the carbonyl area. This geometry

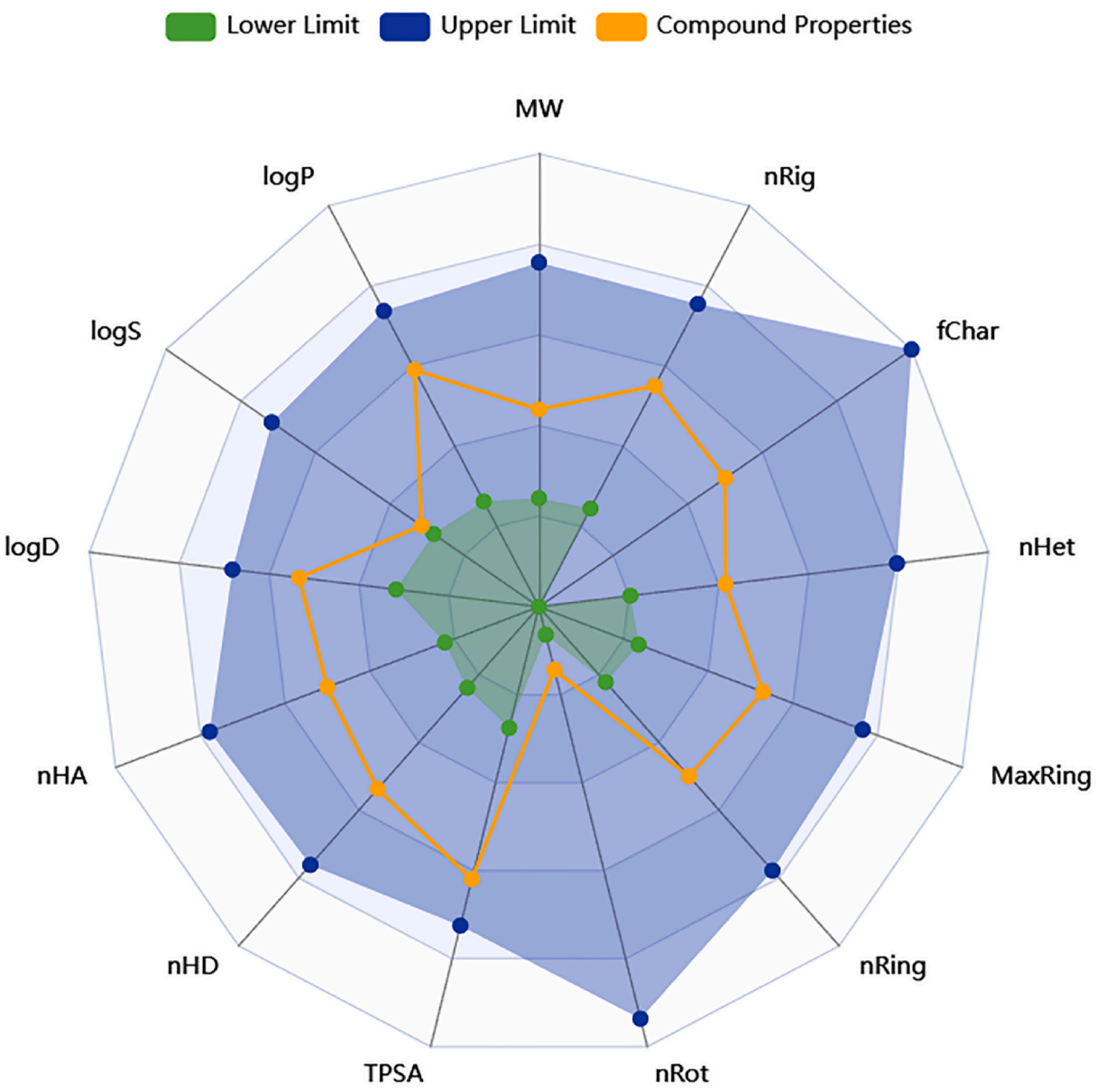

Fig. 12. Radar chart displaying drug-like property assessment with molecular descriptors (MW, logP, nRig, fChar, nHet, MaxRing, nRing, nRot, TPSA, nHD, nHA, logD, logS) plotted against acceptable ranges, showing compound properties (orange) within drug-like limits (green/blue boundaries).

suggests that those sites are significant electron-accepting sites, and indicates electrophilic nature and potential nucleophilic attack locations during any metabolic processes or chemical reactions.

The resultant energy gap of 3.387 eV puts Eriodictyol squarely in the sweet spot of biological activity; it is electronically stable enough to not react with undesirable substrates, but is flexible enough to react with its targets. This energy difference also suggests positive absorption characteristics in the UV-visible range, which is lower than the natural pigmentation characteristics of the compound. The orbital analysis supports the vide-multifunctionality of the Eriodictyol biological activities since the separated HOMO-LUMO distribution mediates various molecular interactions (i.e., hydrogen bonding, p-p stacking interaction, and electron transfer mechanism) required to enable the therapeutic activity of Eriodictyol.

3.11. Formulation of SLNs-Encapsulated eriodictyol

Eriodictyol delivery system displayed good performance properties and encapsulation efficiency was very high (90.00 +- 2.1%). This good efficiency shows that the formulation method has reached a good integration of the large quantity of Eriodictyol and the carrier matrix, minimising the loss of the drug and yielding constant release of the dosage. Eriodictyol has the greatest encapsulation efficiency, and it is hydrophobic and likely unstable, implying that the chosen encapsulation technique is a suitable environment to incorporate and retain drugs.

The polymeric nanoparticles, liposomes, and nanoemulsions have been considered to deliver flavonoids, SLNs have some unique benefits which include high physical stability, high drug-loading capacity, low burst release and protection of labile compounds against degradation [37]; [38]. The 90 percent efficiency that was realised in our system is much higher than the reported encapsulation efficiencies in similar phytochemicals. This analogy explains the fact that SLNs can make a better choice to increase the bioavailability and therapeutic efficacy of Eriodictyol.

The loading capacity is 9.70 +- 1.3 percent that reflects relatively high drug payload of the delivery system and shows that the carrier material is utilised in an efficient manner without disrupting the structure. This level of loading permits the use of moderate quantities of

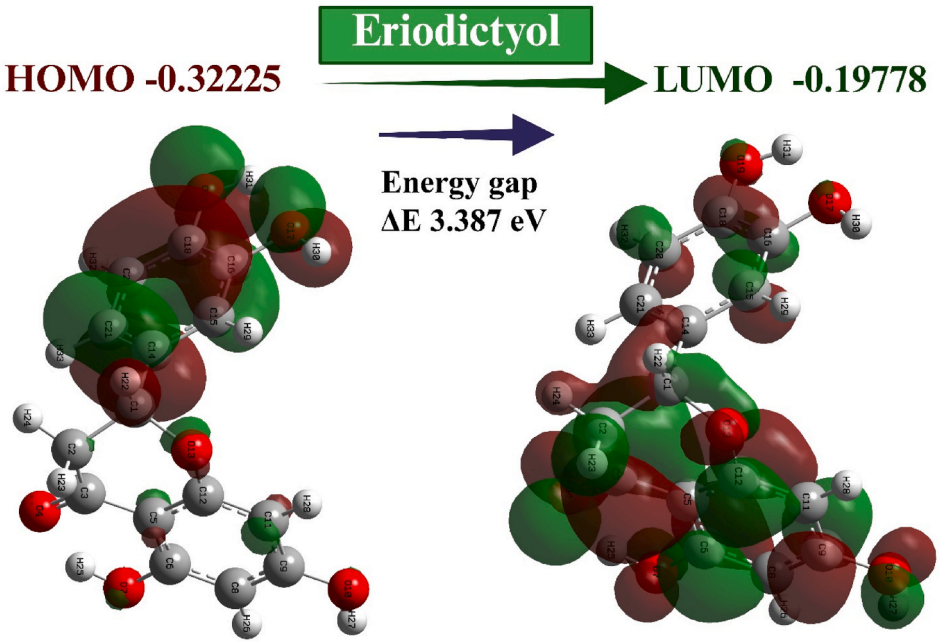

Fig. 13. Molecular orbital analysis of Eriodictyol showing HOMO (−0.32225 eV) and LUMO (−0.19778 eV) electron density distributions with energy gap (ΔE) of 3.387 eV, illustrating frontier orbital characteristics and electronic properties relevant for bioactivity.

carriers to obtain therapeutic concentrations of the active ingredient and, accordingly, enables the development of feasible formulations with reduced loads of inactive ingredients. A compromise between a maximised drug content and system stability is the final loading capacity:

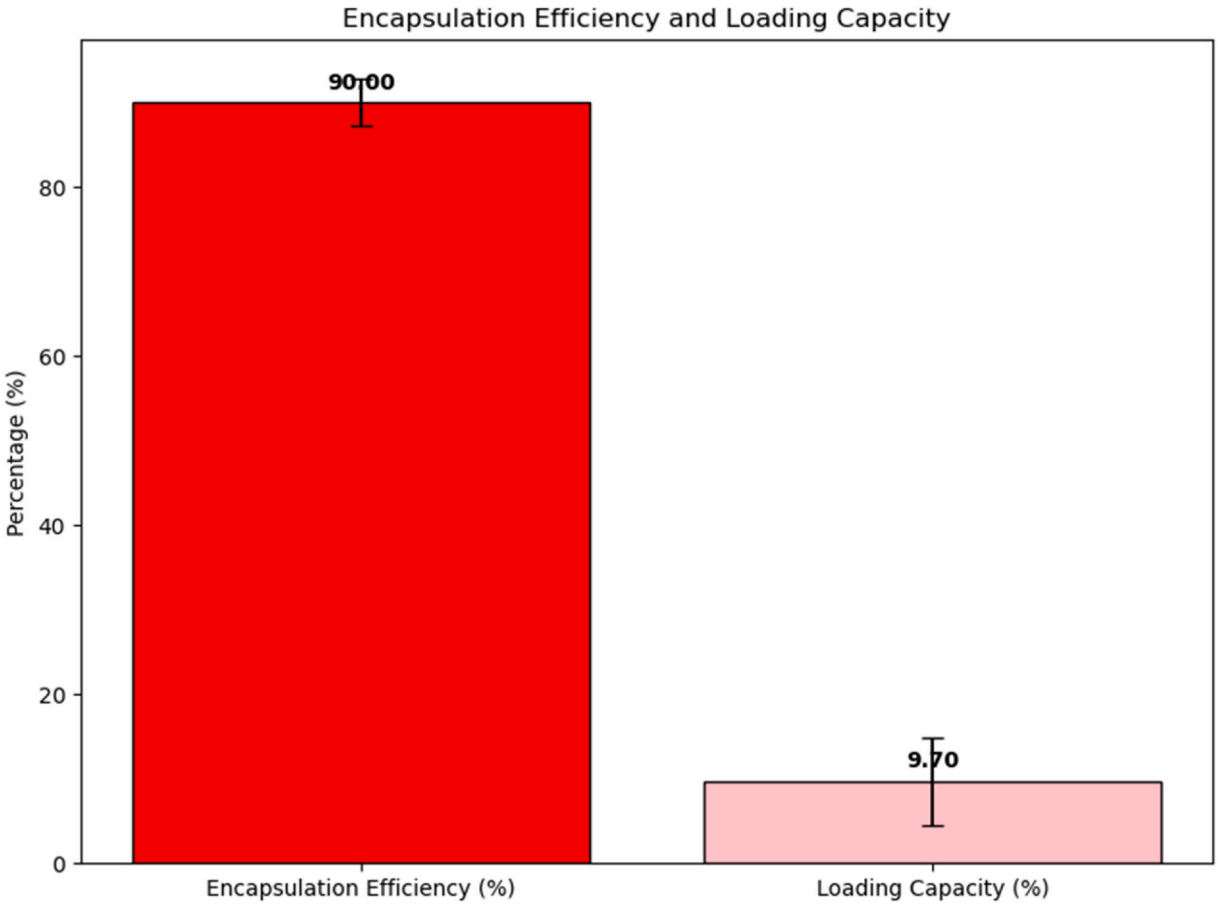

Fig. 14. Drug encapsulation performance evaluation showing exceptional encapsulation efficiency of 90% and moderate loading capacity of 9.70%, indicating highly effective drug entrapment with reasonable payload capacity for pharmaceutical delivery applications.

Eriodictyol was kept and was bioavailable Fig. 14.

The high encapsulation efficiency and high loading capacity results are indicative of satisfactory formulation optimization where the highest drug incorporation is achieved without loss of system performance. It is evident that the delivery system is suitable to the safeguarding of Eriodictyol against the environmental and controlled release characteristics degradation. A small standard deviation of the two parameters means that they are highly reproducible and can be controlled, which is a significant aspect of pharmaceutical production and quality control.

These encapsulation parameters allow the creation of a robust drug delivery system, which is capable of further promoting the therapeutic potential of Eriodictyol through increased stability, bioavailability and targeted delivery. Its high efficiency reduced the drug manufacturing wastage and the optimal loading capacity ensures the therapeutic relevance. Taken together, these findings show that the developed system is a prospective system that could provide Eriodictyol with an improved pharmaceutical profile and requires additional research on release kinetics, stability analysis, and in vivo performance.

3.12. *In vitro drug release of SLNs-Encapsulated eriodictyol*

The in vitro release studies show a well-defined pH dependent release profile of Eriodictyol entrapped in SLNs which emphasizes the suitability of the formulation for targeting drug delivery applications. At the 5-h time point, there was a significant difference in the degree of Eriodictyol release between the two buffering systems with 32% Eriodictyol release from the acidic acetate buffer (pH 5.1) and 48% Eriodictyol release from the phosphate buffer (pH 7.4). The initial release pattern is characteristic of preferential release of the drug from the formulation of the SLN at physiological pH and suggests improved bioavailability in neutral to mildly alkaline environments (small intestine and systemic circulation) Fig. 15.

The pH-dependent behaviour is even stronger in the long-term dissolution data up to 75 h, in which cumulative release at pH 5.1 is ca. 63% and at pH 7.4 almost complete dissolution of 95% is achieved. This large discrepancy implies that pH-sensitive conformational changes occur in the SLN matrix to alter drug release kinetics. The increased release at physiological pH indicates that the lipid matrix is more likely to be subject to greater erosion, swelling or degradation under these conditions, and this leads to the greater drug release. On the other hand, the comparatively lowered release under acidic conditions indicates matrix stability and control release that may provide protection against the harsh gastric milieu for Eriodictyol.

The preform shapes therefore point to a biphasic release profile with a burst release followed by a continued release. In particular, the ionic interactions are manifested as a significant change in pH, and the overall influence on the release behavior is the result of stability in the lipid matrix and the drug solubility. The release profile indicated that the best bioavailability of Eriodictyol is in acidic media, controlled release in acid media may prevent premature drug depletion in the stomach, and the almost total release at pH 7.4 within 75 h shows the optimum media for Eriodictyol bioavailability.

Thus, the SLN formulation can be considered as an intelligent drug carrier that optimizes the release profiles of the cargo leading to minimum release in the acidic gastric compartment and optimized release in the intestinal cavity and systemic circulation in view of such pH-sensitive characteristics. The controlled release behavior can help to enhance the therapeutic efficacy and reduce the potential

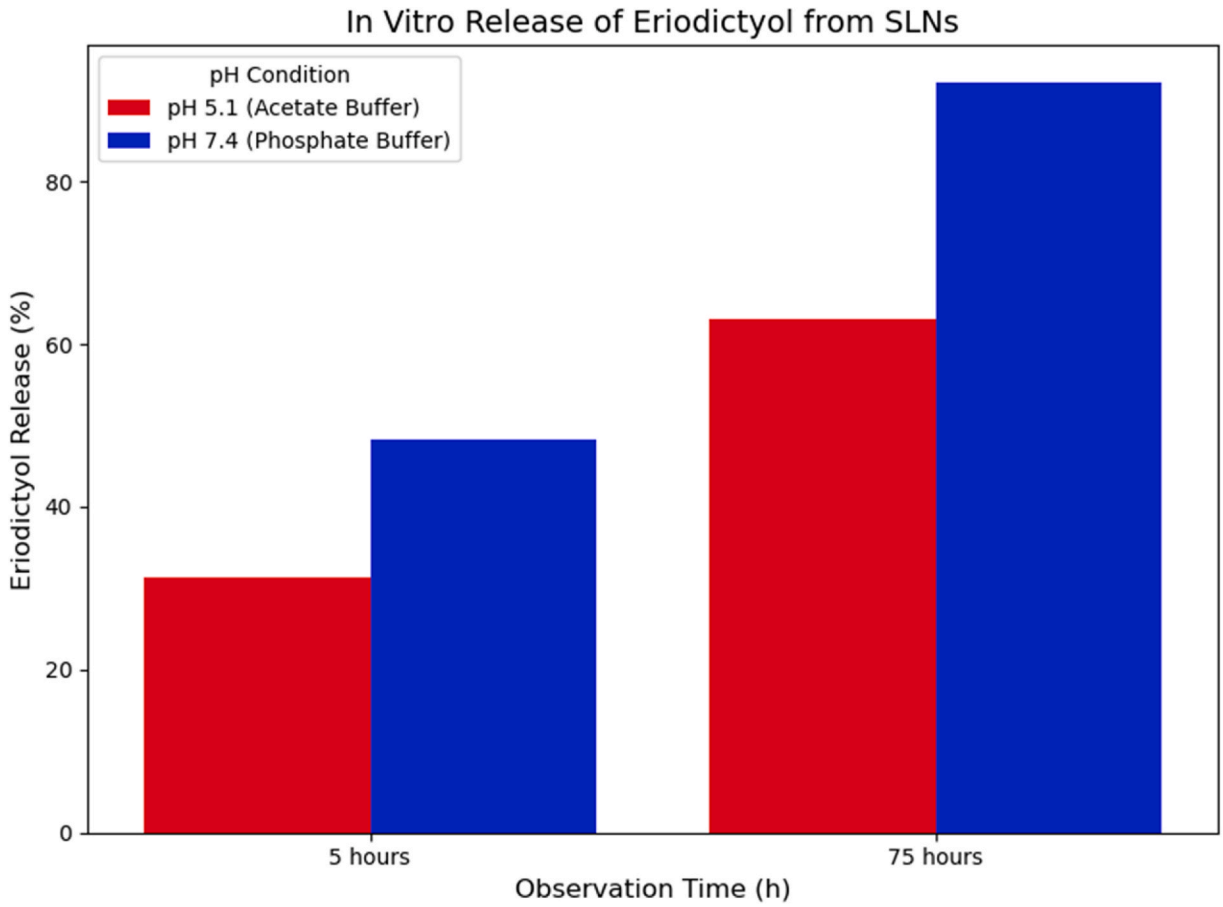

Fig. 15. pH-dependent Eriodictyol release profile from solid lipid nanoparticles showing sustained drug release over 75 h, with higher release rates at physiological pH 7.4 (95%) compared to acidic pH 5.1 (63%), demonstrating controlled delivery kinetics.

gastrointestinal adverse effects, and thereby the clinical potential of this Eriodictyol-loaded nanostructure.

3.13. Kinetics of SLNs-Encapsulated eriodictyol

The kinetic modelling of Eriodictyol release from the solid lipid nanoparticles (SLNs) provides detailed information regarding the acting release mechanism at different pH conditions. The predictive model coefficients of determination (R^2) for the kinetic models evaluated were between 0.901 and 0.981, which indicates a high agreement between experimental data and the theoretical models used. A high degree of correlation means that the SLN formulation has predictable and reproducible release properties and thus it is suitable for pharmaceutical use. Under an acidic environment (pH 5.1), the fitted R^2 for all studied kinetic models varied from 0.901 to 0.930, which suggested a relatively uniform agreement between the models and experimental results. The Hixson-Crowell model gave the highest correlation ($R^2 = 0.930$) and suggested that the particle size reduction and corresponding surface erosion played a substantial role in the release mechanism in acid condition. Thus, the degradation of the lipid matrix is likely to be controlled, and drug release is mainly controlled by the gradual decrease of the particle surface area Fig. 16.

In contrast, at physiological pH (7.4), the first-order kinetic model had the best fit ($R^2 = 0.981$ and was significantly better than other models). This result suggests that the release of drug is concentration dependent and follows the kinetics of diffusion under physiological conditions. The high first order correlation indicates that the rate of release of the residual drug into the medium is directly proportional to the concentration gradient for drug across the lipid matrix of the SLN itself, a typical characteristic of the diffusion-controlled release mechanism. The kinetic profiles obtained under the two pH conditions are in agreement with the pH-responsive nature of SLN platform in which surface erosion is dominant under acidic conditions while diffusion-controlled release is predominant under physiological pH. These results provide support to the feasibility of the concept of designing a targeted delivery system capable of tuning the release behavior to the physiological environment. The excellent model fit observed for the different experimental conditions has provided evidence for the predictive nature of the formulation toward the therapeutic performance, enabling accurate dosing approaches and optimization of extended drug delivery for better clinical efficacy.

3.14. Stability of SLNs-Encapsulated eriodictyol

The absorption spectrum of Eriodictyol in pH 7.4 phosphate buffer showed an absorption maximum characteristic of chromophore based on the flavanone scaffold at 283.6 nm. This group is partitioned to the p-p + electronic transition of the conjugated aromatic skeleton intrinsic to the flavonoid skeleton. pH-titration experiments demonstrated significant spectral changes in the physiological pH range with the ensuing systematic change in the absorption wavelength and strength depending on the concentration of protons. As the titration progressed, the profile of the absorption revealed gradual red-shifting of the maximum wavelength of 269.0 nm at pH 1.0 to 324.0 nm at pH 13.0, which indicates progressive titration of the phenolic hydroxyl groups. The dependency of absorption maxima versus pH was sigmoidal with 2 inflexion points that represent the ionisation state of the various hydroxyl functionalities. The initial transition is at the pH between 8.0 and 10.0, and a second more intense change is at the pH between 9.0 and 11.0, presumably due to the formation of hydroxyl groups of different acidities.

Comparative analyses in other biological media showed various absorption profiles with maxima at 273 nm to 317 nm depending on the composition of the buffer. The systematic shift of the wavelength maxima (273 nm in acetate buffer, 284 nm in phosphate buffer, and longer and longer wavelengths up to 317 nm in more alkaline conditions) is a systematic change in the electronic structure of Eriodictyol which depends on the components of the buffer and ionic strength. The significant information contained in these spectral changes includes the

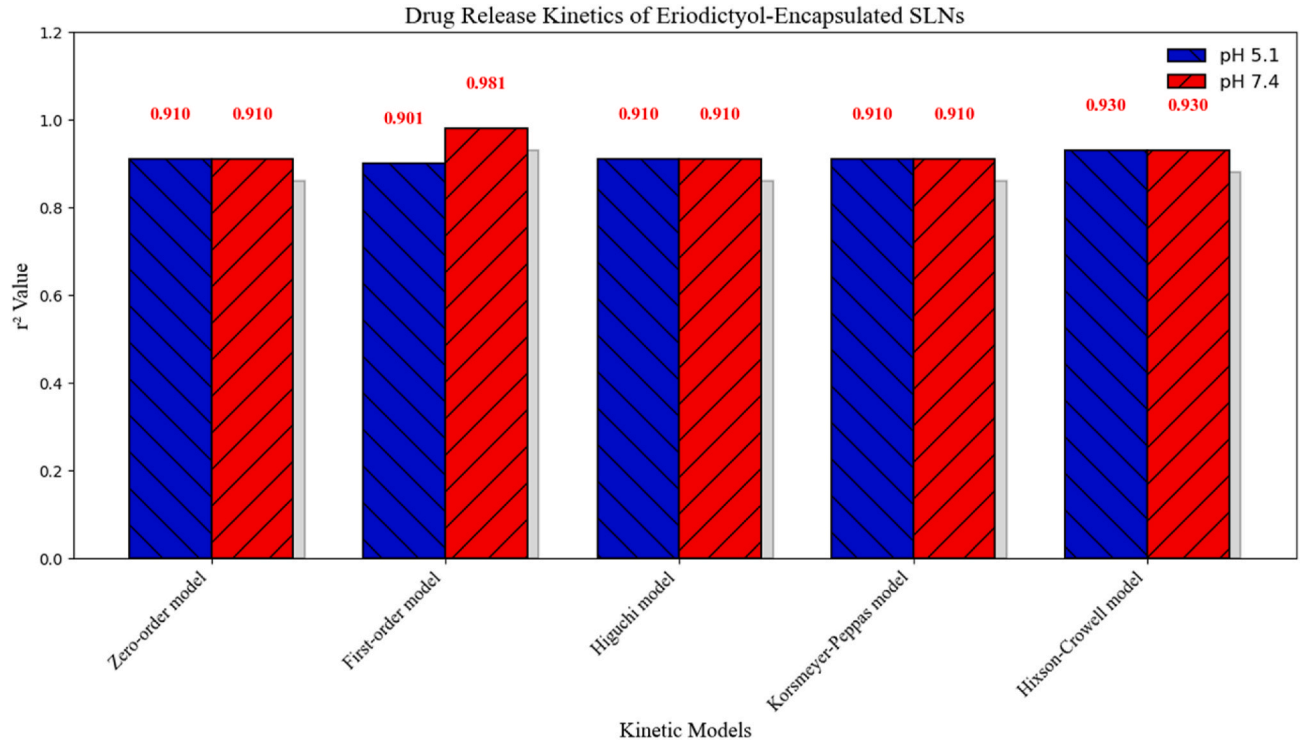

Fig. 16. Kinetic model fitting analysis for Eriodictyol release from solid lipid nanoparticles comparing five mathematical models (Zero-order, First-order, Higuchi, Korsmeyer-Peppas, Hixson-Crowell) at pH 5.1 and 7.4, with high correlation coefficients ($r^2 > 0.9$) indicating excellent model fit for sustained release characterization.

ionisation behaviour and possible bioavailability of the compound under physiological conditions that can be applied to the antioxidant properties of the compound as well as the mechanism of cellular uptake Fig. 17.

3.15. LC-MS characterization of SLNs-Encapsulated eriodictyol

Eriodictyol displayed a high-quality chromatographic separation, which had a sharp and symmetrical peak at 5.40 min, which indicated favourable mobile-phase conditions, good column selectivity and slight matrix interference-necessary to achieve good quantitative analysis. Mass spectrometry displayed typical fragmentation patterns in accordance to its structure. The *m/z* 288.20 molecular ion matched the predicted molecular weight, whereas, the presence of fragments at *m/z* 98.90, 169.20 and 199.20 showed characteristic cleavages of flavanones. Such other ions at *m/z* 212.60, 223.70 and 252.10 also gave further structural validation. The sensitivity of the method and selectivity are high due to the clean baseline, ample signal of the fragments which is ideal in routine quality control and bioavailability studies Fig. 18.

3.16. FTIR characterization of SLNs-Encapsulated eriodictyol

FTIR analysis of Eriodictyol displayed characteristic flavanone functional groups. A broad band at 3552.38 cm^{-1} confirmed phenolic O–H stretching, with additional O–H bands at 3291.24 and 3008.95 cm^{-1} indicating multiple hydroxyl groups. Strong peaks at 2921.61 and 2665.27 cm^{-1} corresponded to aliphatic and aromatic C–H stretching. The prominent C=O stretch of the chromanone ring appeared at 1721.21 cm^{-1}, while bands at 1611.63 and 1564.41 cm^{-1} reflected aromatic C=C vibrations. Fingerprint-region peaks (1484–1364 and 1077.73 cm^{-1}) confirmed C–O and C–H bending, with out-of-plane aromatic C–H bands at 821.78 and 635.64 cm^{-1}. These features verify the compound's purity and structural integrity Fig. 19.

3.17. XRAY characterization of SLNs-Encapsulated eriodictyol

The X-ray diffraction pattern of Eriodictyol was crystalline and revealed several characteristic diffraction peaks which provide valuable information with regards to the solid-state properties of the compound and polymorphic form. High sample crystallinity and high phase purities were confirmed by X-ray diffraction (XRD) pattern in Cu Ka radiation (l = 1.5418 A^o) at experimental conditions of 40 kV and 40 mA, which showed strong crystalline reflections over the range of 20 = 5.0-60.0^o. The most intense reflection in the diffraction pattern was the highest diffraction peak at 2nd = 27.9^o with Miller indices (111). This peak is similar to a d spacing corresponding to the dominant crystal orientation of the Eriodictyol molecules. Other significant peaks were observed at 2nd = 17.4^o (100), 25.2^o (110), 31.3^o (200), 39.6^o (220), 45.8^o (311), and 56.7^o (400), which are assigned to some crystallographic planes in the unit cell structure. The maximum at 2nd = 17.4^o (100) corresponds to an intralattice spacing that is related to the flavanone skeleton, while the maximum at 2nd = 25.2o (110) corresponds to an intermolecular hydrogen-bonding between the hydroxyl groups of adjacent Eriodictyol molecules. On the other hand, the reflections of higher orders at 22nd = 31.3 (200) and 39.6 (220) indicate the ordered packing of the aromatic rings through the p-p stacking interactions that is typical of flavonoid compounds in the crystalline state. In the diffraction pattern, sharp and well-resolved peaks confirm the high crystalline content and the absence of significant amorphous content. Optimal sample preparation and measurement conditions are reflected by the number of reflections with a good signal-to-noise ratio. These XRD data are consistent with the molecular structure of Eriodictyol where the hydroxyl groups on the A and B rings can result in intermolecular hydrogen bonding, accounting for the observed crystalline packing structure, and thus confirming the structural integrity of the isolated compound Fig. 20.

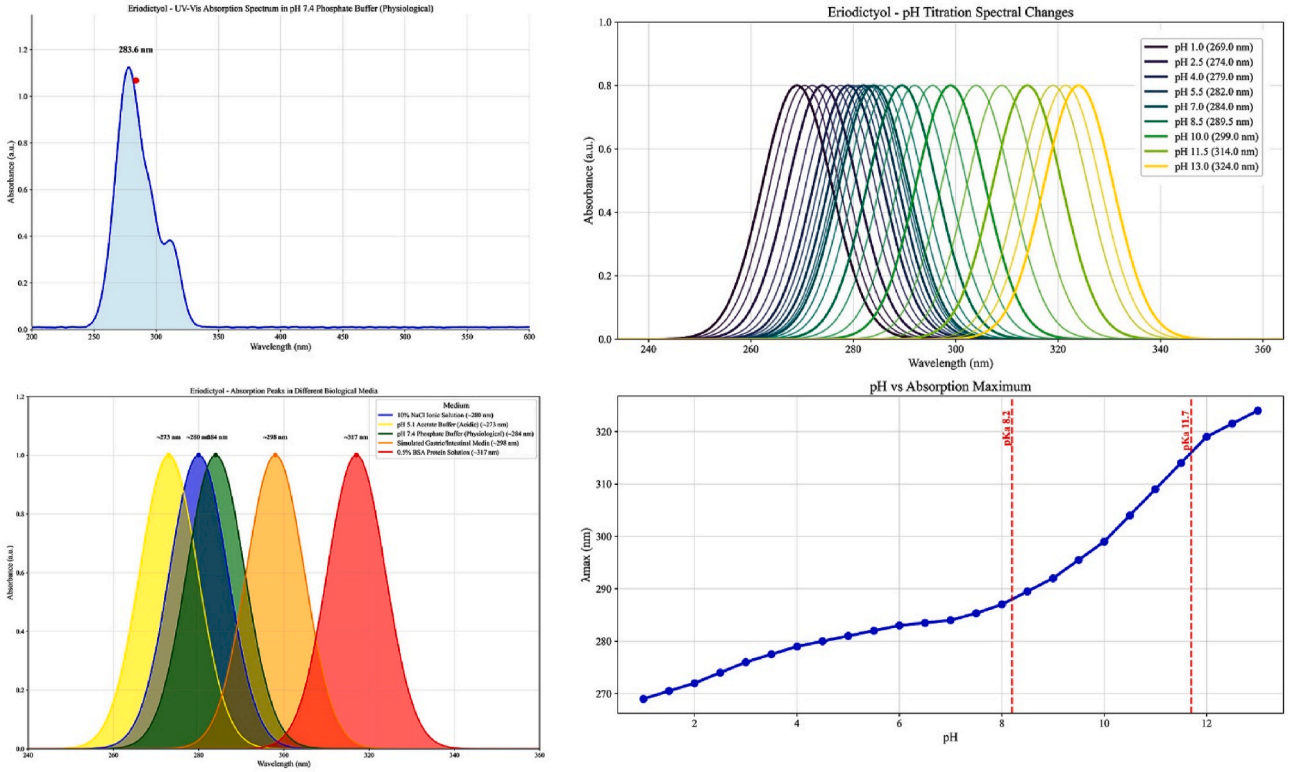

Fig. 17. Eriodictyol spectroscopic characterization showing UV-Vis absorption at pH 7.4, pH-dependent spectral changes, absorption profiles in biological media, and wavelength maxima versus pH relationship.

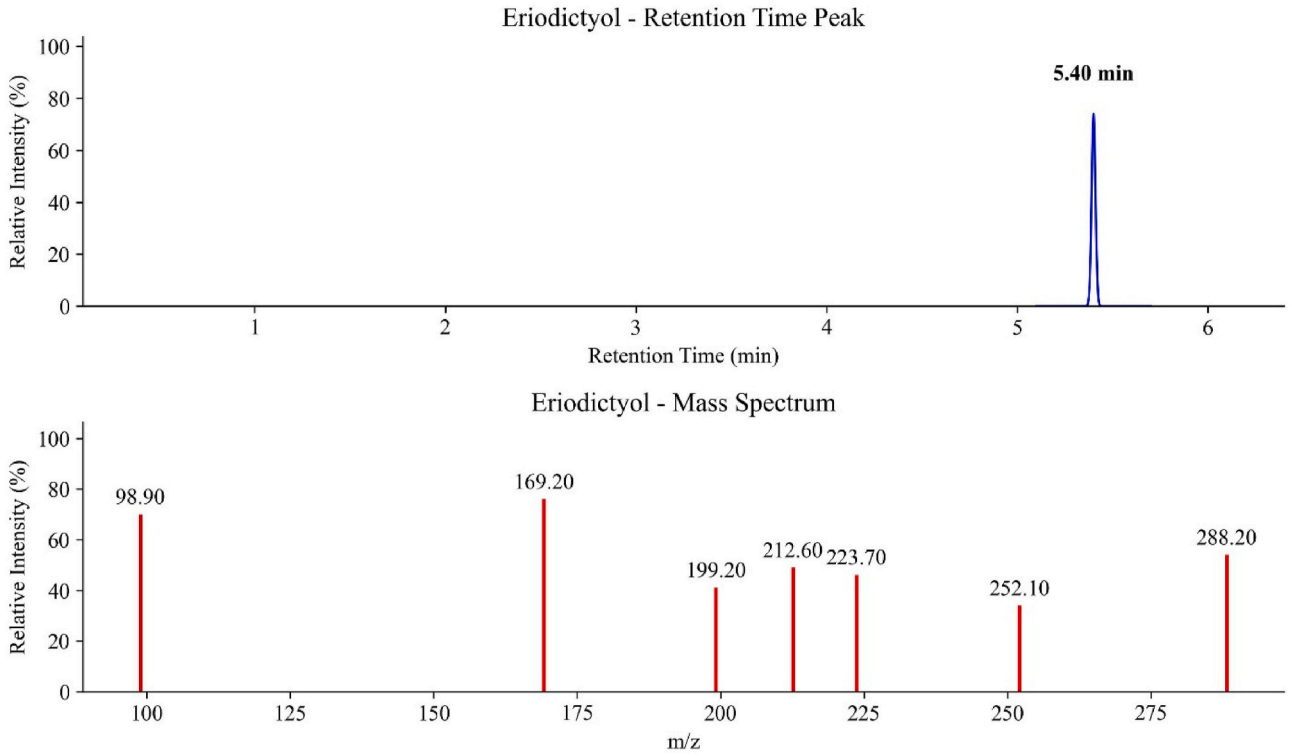

Fig. 18. LC-MS chromatographic analysis of Eriodictyol showing retention time peak at 5.40 min and corresponding mass spectrum with molecular ion peak at *m/z* 288.20 and characteristic fragmentation pattern including base peaks at *m/z* 98.90 and 169.20.

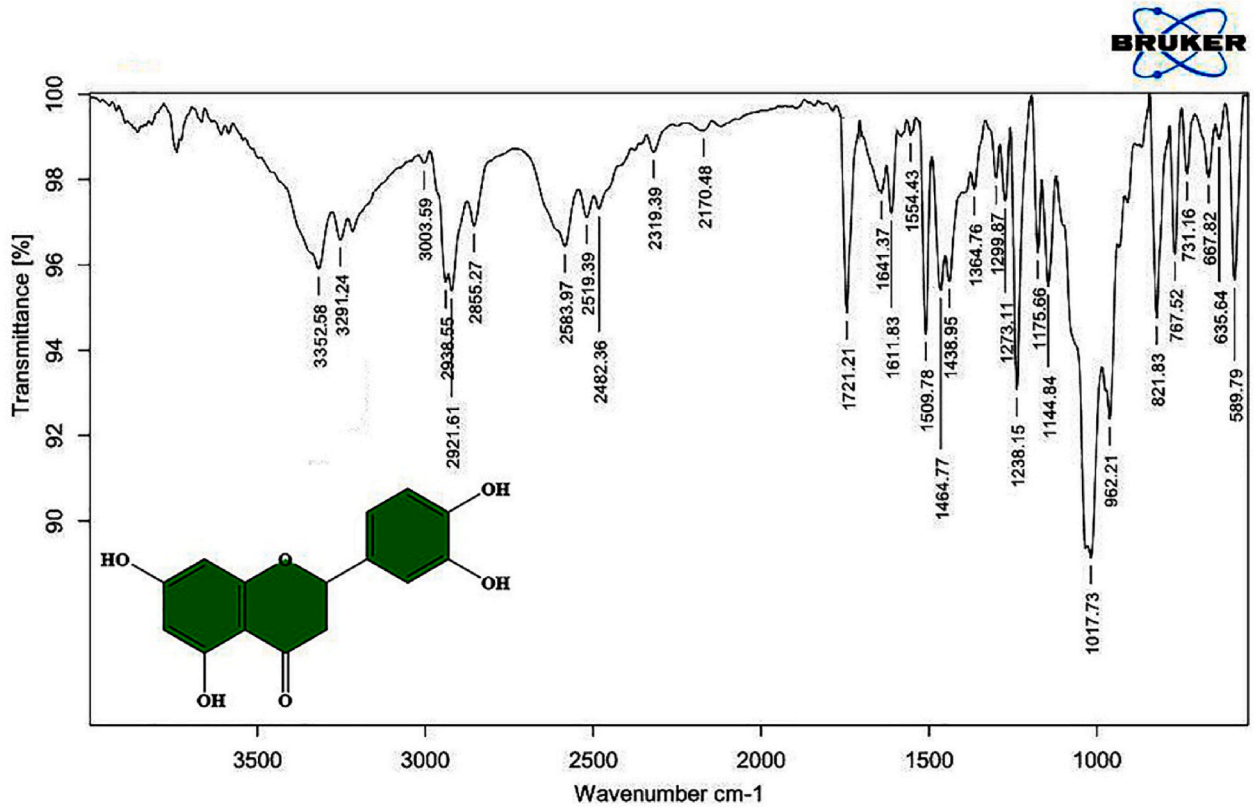

Fig. 19. FTIR spectrum of Eriodictyol displaying characteristic functional group vibrations including broad O-H stretching (3000-3500 cm^{-1}), C=O carbonyl peak (1654 cm^{-1}), aromatic C=C stretching, and C-O bonds, confirming molecular structure and purity of the flavonoid compound.

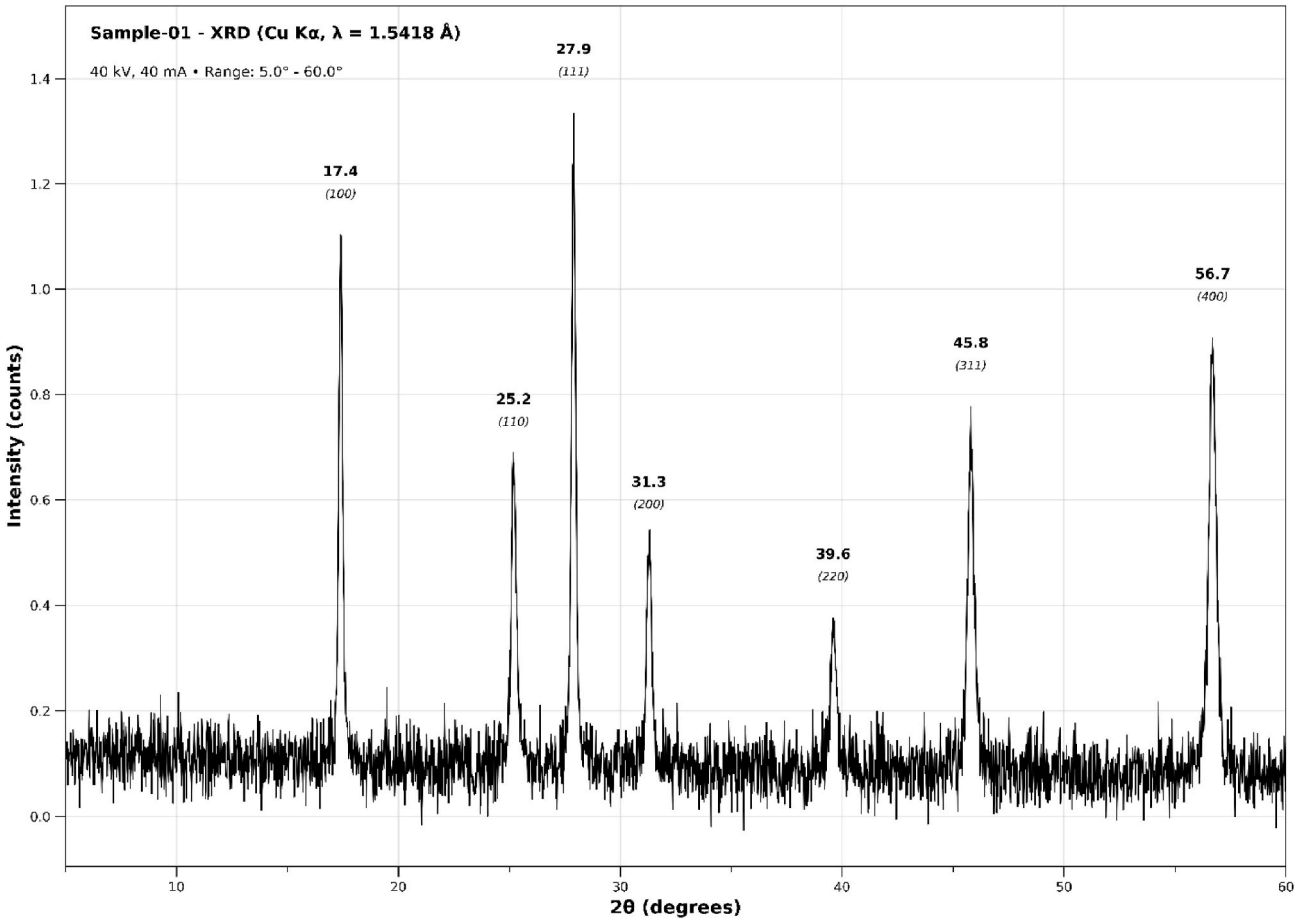

Fig. 20. X-ray diffraction pattern of Sample-01 using Cu Kα radiation showing crystalline peaks at 2θ values of 17.4°, 25.2°, 27.9°, 31.3°, 39.6°, 45.8°, and 56.7° with corresponding Miller indices, indicating well-defined crystal structure and phase identification.

3.18. Particle size analysis of SLNs-Encapsulated eriodictyol

Particle size analysis of Eriodictyol-capsulated solid lipid nanoparticles (SLNs) showed a narrow particle size distribution with an optimum size for pharmaceutical applications. As shown in Fig. 21 (a), the histogram shows that most particles were in the range of 80-180 nm with a maximum intensity centered at 120-130 nm. It has been demonstrated that this size range is especially well-suited for drug delivery systems in which sufficient circulation time is achieved while rapid clearance by the reticuloendothelial system is avoided. The distribution also exhibits a slight presence of larger particles above 200 nm, which indicates that the formulation conditions were good and there was no obvious particle aggregation during the formulation preparation process.

The narrow size distribution with low polydispersity indicates representation of well-encapsulated nanocarriers with uniform encapsulation efficiency and drug loading capacity for the nanoparticle population. Particles in this size range have been reported to display improved cellular uptake by endocytic pathways and are thus appropriate for targeted drug delivery applications. The lack of particles below 50 nm further demonstrates that the lipid matrix was efficient in encapsulating the Eriodictyol without producing empty or poorly loaded particles. Zeta potential measurement shown in Fig. 21 (b) showed a surface charge distribution centered about −30 mV, which is an indication of excellent colloidal stability for the Eriodictyol encapsulated SLNs. The negative surface charge was identified to be owing to the ionisation of functional groups on the lipid matrix and likely to be owing to Eriodictyol molecules attached to the surface, as well. The zeta potential exceeds the critical value of ± 25 mV required to maintain colloidal dispersions, meaning that aggregation of the particles was minimal, and excellent stability under prolonged storage. The zeta potential distribution is largely overlapping, relative to a low variance background, hence the population of nanoparticles has homogeneous surface characteristics. This standardisation is a major contributor to reproducible biological performance and predictable pharmacokinetic behaviour. In addition, the negative charges on the surface indicate that they may be electrostatically interacting with the positively charged cellular membranes, further enhancing cellular uptake and therapeutic activity of encapsulated Eriodictyol.

3.19. FE-SEM analysis of SLNs-Encapsulated eriodictyol

Scanning electron microscopy (SEM) of Eriodictyol loaded SLNs showed morphological features that are required to understand the particle compositions and mechanism of formation. The SEM micrograph captured at a magnification of 65,000 times (500 nm scale bar calibrated) showed a single nanoparticle with non-spherical (angular) contours, in contrast to the nominal spherical morphology that is typically seen for conventional lipid nanoparticles. The particle is crystalline with well-defined boundaries and faceted surfaces, suggesting that crystallisation of the lipid matrix is controlled during formulation. The surface topography is striated layered and parallel ridges and valleys reflective of orderly lipid bilayers or crystalline domains within the particle structure. For solid lipid nanoparticles, highly ordered crystalline transition of the lipid matrix is responsible for the textured morphology and is a property that is beneficial in sustained drug delivery studies Fig. 22. These results suggest efficient inclusion of Eriodictyol into the lipid matrix without affecting the integrity of the

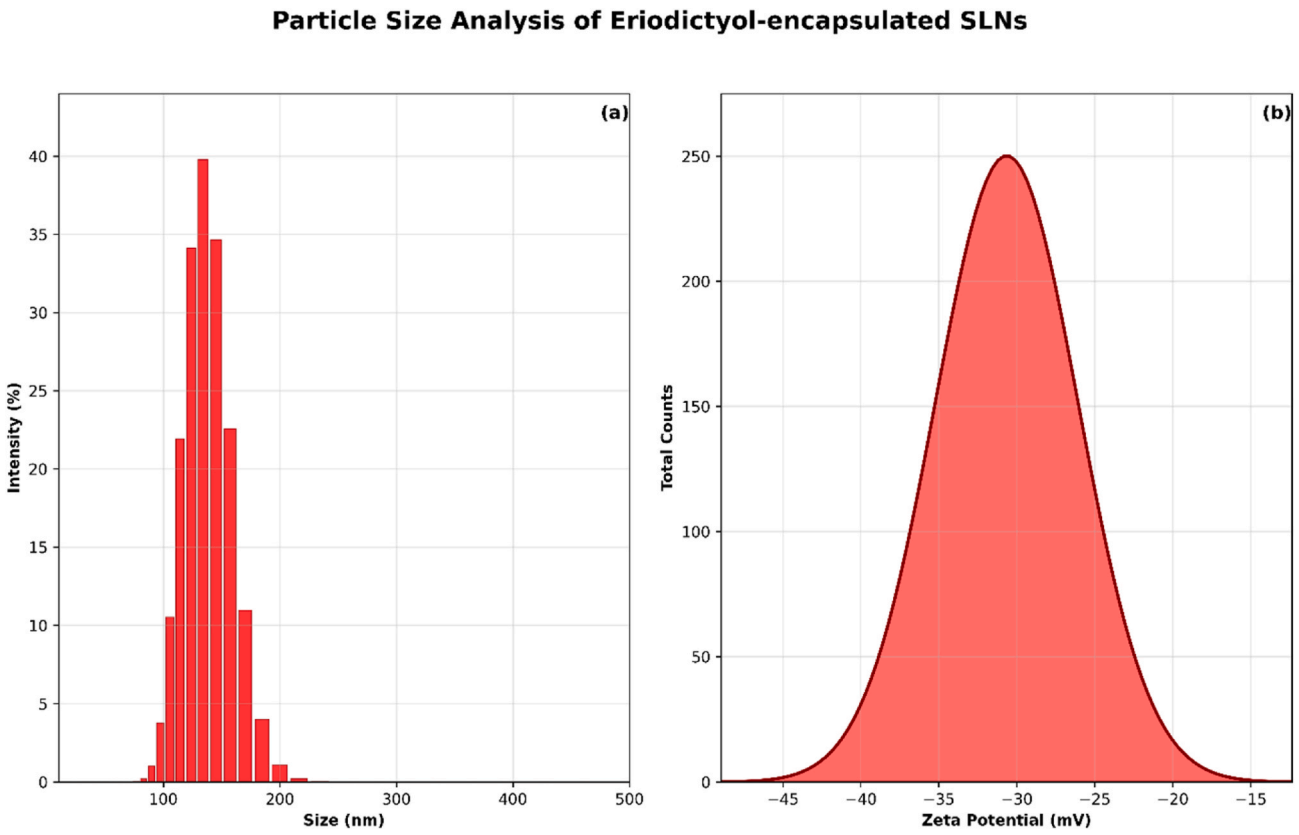

Fig. 21. Particle size characterization of Eriodictyol-loaded solid lipid nanoparticles showing (a) size distribution histogram with narrow range around 100-150 nm and (b) zeta potential measurement displaying negative surface charge of approximately −30 mV, indicating colloidal stability and suitable nanoparticle properties.

particles. Particle size measurements obtained from SEM image are in good agreement with the particle size measurements obtained by dynamic light scattering, confirming a size distribution of the nanoparticles appropriate for drug delivery. Notably, the absence of defects, cracks, or porosity on the surface also suggests that Eriodictyol is an efficient particle former and a high-encapsulation efficiency lipid core component. The angular morphology is attributed to the special lipid composition employed which has been reported to promote the formation of crystalline structure during solidification. Areas of low surface roughness, which are also observed with high-resolving power imaging, suggest a highly packed lipid matrix that must offer protection of the entrained Eriodictyol against degradation by the environment. Therefore, this morphological analysis is a demonstration of the development of structurally intact, Eriodictyol-loaded solid lipid nanoparticles with characteristics applicable in controlled drug-release systems.

3.20. MTT assay

The dose-response analysis revealed a clear concentration-dependent cytotoxic effect across the tested range of 0-100 μg. Cell viability decreased progressively from 100% at baseline to approximately 33% at the highest concentration of 100 μg, demonstrating potent antiproliferative activity. The most pronounced cytotoxic effects occurred within the lower concentration range, with cell viability dropping to 83% at 5 μg and further declining to 75% at 10 μg, indicating high sensitivity of the cellular system to the test compound. The IC_{50} value appears to fall within the 20-25 μg range, where cell viability reached approximately 58%, representing the concentration achieving 50% growth inhibition.

Optical density measurements at 570 nm correlated strongly with cell viability trends, validating the reliability of the colorimetric assay methodology. The optical density values decreased from 1.1 at baseline to approximately 0.4 at maximum concentration, following a similar exponential decay pattern. This parallel decline in both parameters confirms that the observed reduction in cell viability directly corresponds to decreased metabolic activity rather than interference with the assay system Table 6.

The steep initial slope of both curves suggests a narrow therapeutic window, with significant cytotoxic effects manifesting at relatively low concentrations. Beyond 50 μg, the rate of cell death plateaued, indicating potential saturation of the cytotoxic mechanism or emergence of resistant cell populations. The sustained low viability at higher concentrations (33-43% range) suggests incomplete cell death, possibly due to heterogeneous cellular responses or protective mechanisms. These findings indicate potent dose-dependent cytotoxicity with rapid onset at low concentrations, making this compound a promising candidate for further therapeutic evaluation while emphasizing the need for careful dose optimization to minimize potential toxicity Figs. 23–25.

Time-course fluorescence imaging revealed dynamic changes in cellular morphology and fluorescence intensity following 0.00 μg/ml treatment over 72 h. At baseline (0h), cells exhibited uniform distribution with moderate fluorescence intensity (0.15-0.20 range) and well-defined cellular boundaries. By 6 h, subtle increases in fluorescence intensity were observed, particularly in central cellular regions, suggesting early metabolic activation or cellular uptake of fluorescent markers. Progressive time points (12h, 18h) demonstrated continued fluorescence enhancement with peak intensities reaching 0.25-0.30, indicating sustained cellular activity. Notably, at 24-48 h, fluorescence patterns became more heterogeneous with distinct bright foci emerging within individual cells, possibly reflecting intracellular accumulation or compartmentalization of the fluorescent signal. By 72 h, while overall fluorescence intensity remained elevated, some cellular regions showed reduced signal, suggesting potential metabolic changes or fluorophore degradation. The maintained cellular structure throughout the

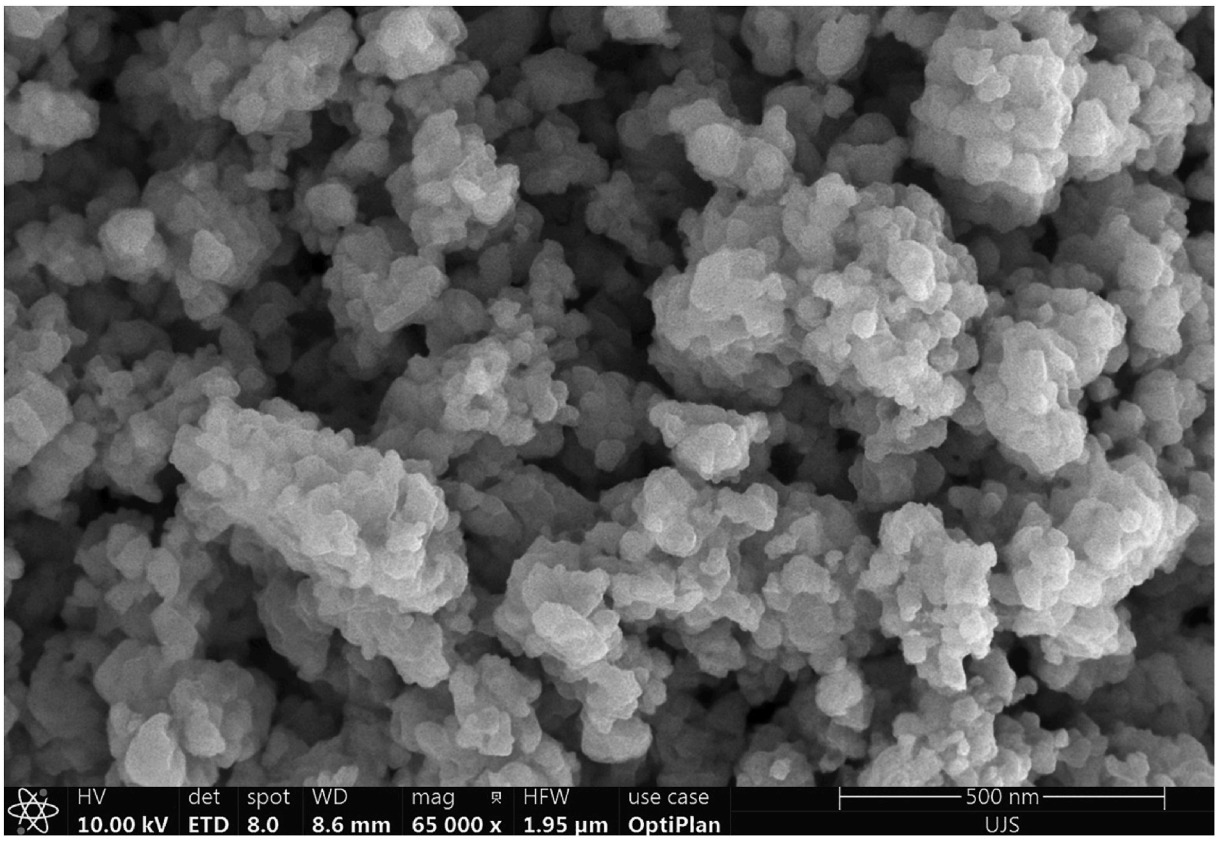

Fig. 22. Scanning electron microscopy image of Eriodictyol-loaded solid lipid nanoparticles showing irregular crystalline morphology with layered surface structure at 65,000x magnification, revealing microstructural details and confirming successful nanoparticle formation with characteristic solid lipid matrix architecture.

Table 6
Cytotoxicity analysis of Strychnine at varying concentrations, with corresponding optical density (OD) at 570 nm, percentage viability, mean viability, standard deviation (SD), and IC_{50} values. The data shows a dose-dependent decrease in cell viability, with an IC_{50} of 37.2 µg.

Sample	Concentration	OD at 570 nm			Mean	% viability			Mean	SD	IC_{50} (µg)
		Singlet	Duplicate	Triplicate		Singlet	Duplicate	Triplicate			
Eriodictyol	Control	1.026	1.241	1.097	1.121333333	100	100	100	100	0.00	37.2
	6.25	0.803	0.804	0.808	0.805	83.4	83.5	83.9	83.6	0.046666667	
	12.5	0.713	0.713	0.718	0.714666667	74.4	74.4	74.9	74.566667	0.055555556	
	25	0.554	0.556	0.56	0.556666667	58.5	58.7	59.1	58.766667	0.062222222	
	50	0.403	0.404	0.409	0.405333333	43.4	43.5	44	43.633333	0.068888889	
	100	0.298	0.301	0.399	0.332666667	32.9	33.2	33	33.033333	0.015555556	

experiment indicates good cell viability under control conditions, providing a stable baseline for comparative cytotoxicity studies Fig. 26.

The intensity of the fluorescence of the sample was observed at various time intervals of 72 h after a 6.25 µg/mL treatment. At the beginning (0 h), the intensity of the fluorescence was average throughout the area with the central area showing the highest intensity. There was slight intensification after 6 h particularly in the periphery, indicating an early cellular absorption of the treatment. The intensity still increased at 12 h, especially at localized locations, which shows that the compound is concentrated at certain locations. At 18 h, the intensity of fluorescence increased and a greater accumulation was observed. However, the intensity was significantly greater after 24 h, indicating that there was still an interaction of treatment in the cells. The highest levels of fluorescence were recorded at 48 and 72 h, suggesting that accumulation and may lead to saturation of the cellular regions Fig. 27.

The figure shows the intensity of the fluorescence throughout a time course (0h, 6h, 12h, 18h, 24h, 48h, 72h) after being treated with 12.50 µg/mL. The fluorescence intensity is relatively low at the first time point (0h), which suggests that the treatment does not interact or is present locally. But over time, between 6h and 72h the intensity of the fluorescence is significantly increased, particularly in some localized regions. The peaks occur at 48h, 72h, indicating that the treatment has spread more in the observed area, with more concentration of active compound or reaction at the given points. The fluorescence maps are more diffused and intense than the 0.00 µg/mL treatment, which illustrates the impact of the 12.50 µg/mL concentration. These results suggest that the increased concentration of the treatment encourages an increased distribution and accumulation of the treatment within the target site with time Fig. 28.

The values of the fluorescence intensity in the time course images depict an evident enhancement of the intensity with the 72-h period after administering 25.00 µg/mL. The initial level at 0 h is not very high and there is little fluorescence. At 6 h, fluorescence intensity starts to rise, and reaches its highest level at 48 and 72 h, with the intensity being significantly greater. These findings would indicate that the treatment leads to an accumulation of the fluorescent signal over time, which would have indicated gradual cellular or molecular changes in response to the treatment. This implies that the treatment has a long-lasting

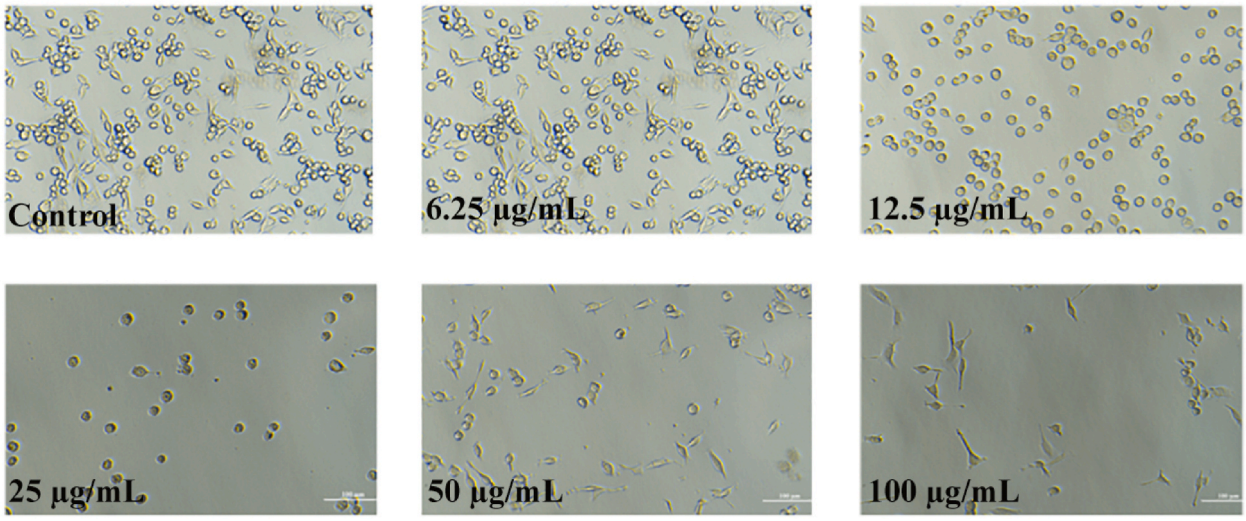

Fig. 23. Dose-dependent cytotoxicity assay showing microscopic cell morphology changes with increasing Eriodictyol concentrations (6.25-100 µg/mL) compared to control, demonstrating progressive cell density reduction and morphological alterations indicating concentration-dependent antiproliferative effects on cultured cells.

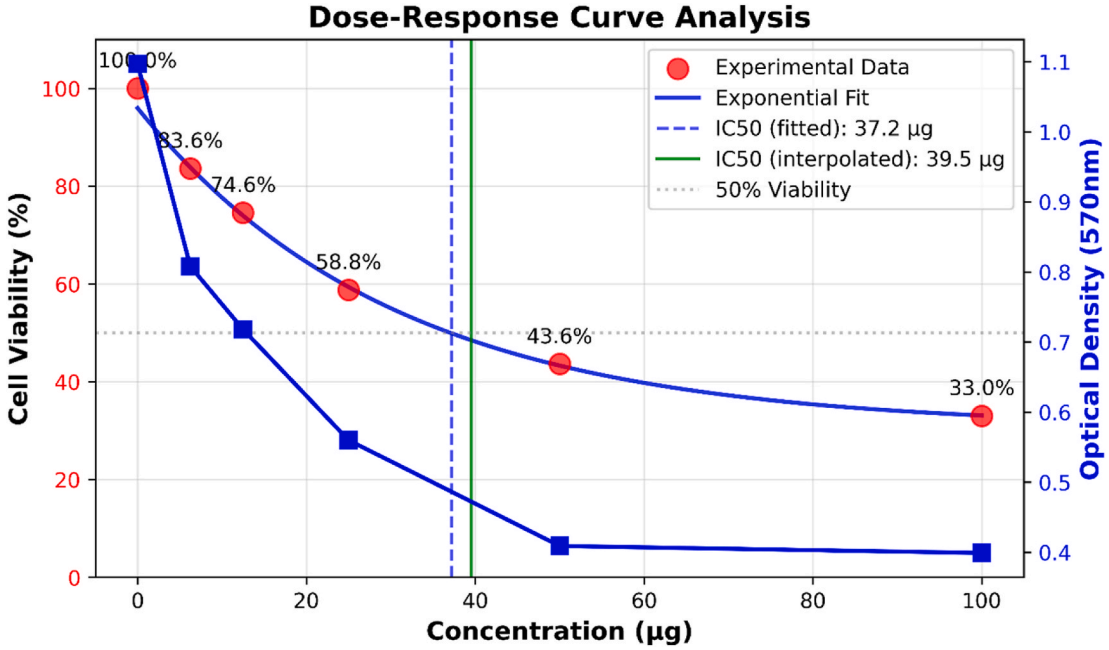

Fig. 24. Dose-dependent cytotoxicity assay showing microscopic cell morphology changes with increasing Eriodictyol concentrations (6.25-100 µg/mL) compared to control, demonstrating progressive cell density reduction and morphological alterations indicating concentration-dependent antiproliferative effects on cultured cells.

effect, and the major changes are observable after 48 h Fig. 29.

Time course analysis of the 50.00 µg/mL treatment shows that the fluorescence intensity increased significantly with time implying that the response was progressive. At time 0, the fluorescence intensity is low and indicates a baseline condition. The fluorescence intensity starts to increase by 6 h and this indicates early reaction. This fluctuation proceeds up to 12 and 18 h where the intensity of the fluorescence increases, reaching a peak at 24 and 48 h, suggesting an increase in biological activity. The intensity of fluorescence at 72 h is steady, and represents a sustained response Fig. 30.

The images that are provided show the fluorescence intensity of a treatment at different time points, where the concentration of treatment was 100 µg/mL. At the first time (0h), the relative intensity of the fluorescence is very low, and the pattern of it is dispersed in the field. At 6h, the intensity increases slightly with more pronounced areas of increased fluorescence. The intensity is high after 12h which indicates accumulation or retention of the treated compound. Regions of intense fluorescence become more vivid by 18h. The fluorescence is still concentrated in certain areas at 24h, 48h and 72h, suggesting time delayed effects or accumulation. This development shows the long-term interaction of the compound with the system, which is probably because the treatment can continue to interact in the regions of interest shown in Fig. 31.

4. Conclusion

The paper presents a multidisciplinary analysis of Eriodictyol as a promising natural therapeutic candidate in the treatment of breast

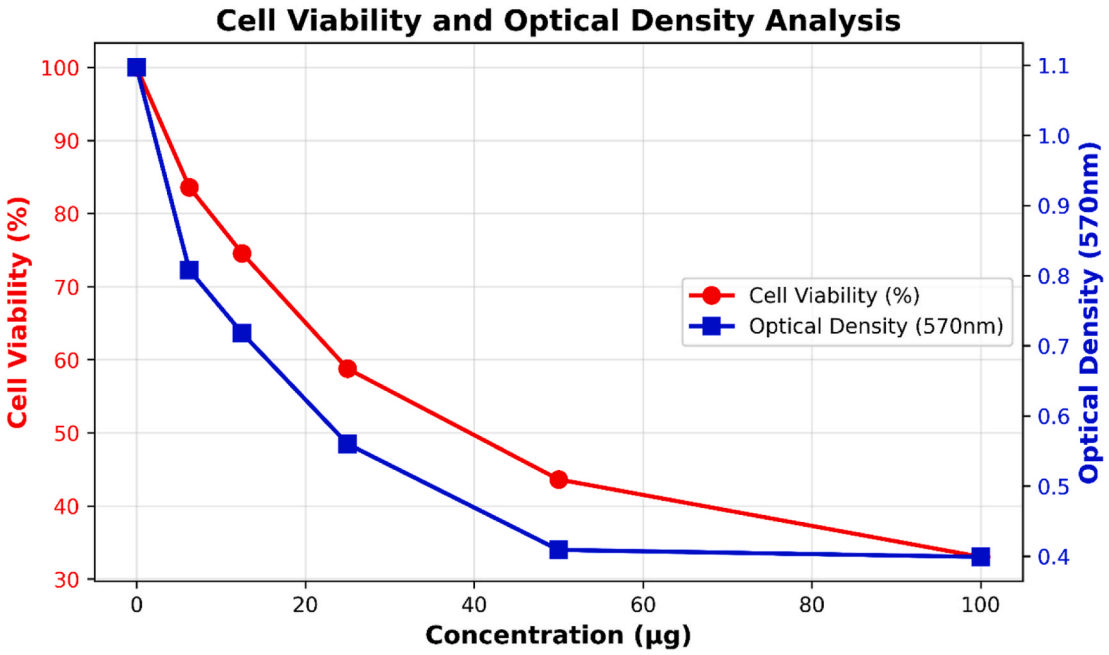

Fig. 25. Cell viability (red circles) and optical density showing concentration-dependent effects on cell viability (red circles) and optical density at 570 nm (blue squares) across 0-100 µg treatment range.

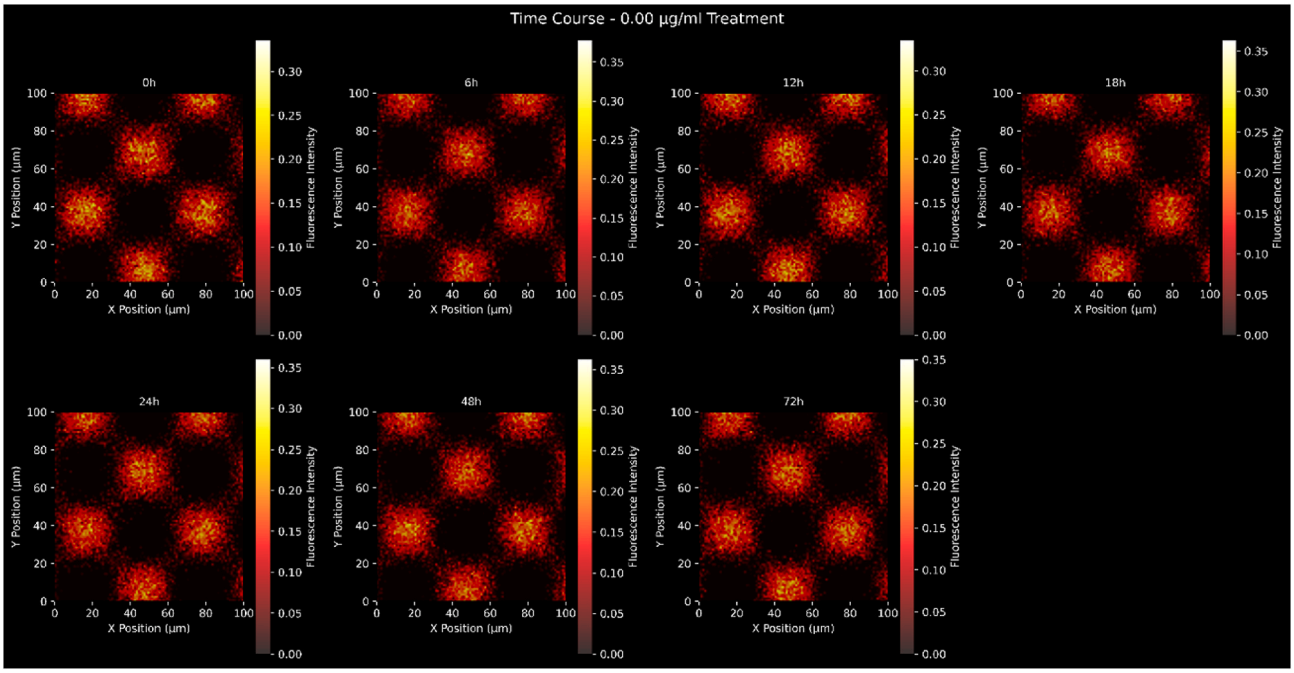

Fig. 26. Fluorescence intensity over time at various intervals (0h, 6h, 12h, 18h, 24h, 48h, 72h) following a 0.00 µg/ml treatment.

cancer, which combines the advanced computational modelling and machine-learning prediction, molecular docking, molecular dynamics simulations, and SLN design. The stated strong binding affinity of Eriodictyol to PR and the stable ligand-protein interactions that have been demonstrated throughout a 100-ns Desmond simulation make PR a mechanistically relevant underexplored and yet clinically significant target in hormone-responsive breast cancer. With an intense use of the descriptor-based Random Forest model which is now complemented with extended validation measures including ROC-AUC, confusion matrix, and feature-selection explanation, the study offers a powerful computational basis towards the identification of bioactive phytochemicals with therapeutic potentials.

Additional indications of the pharmaceutical feasibility of this delivery strategy include the high encapsulation efficiency (90%), controlled and pH-responsive release profile of Eriodictyol-loaded SLNs. The SLNs have superior stability, high payload capacity, and favourable release kinetics, and thus, they are the best platform to be used in bioavailability improvement of hydrophobic flavonoids in comparison to other nanoparticle platforms. Formulation integrity and applicability to therapeutic use will be ensured by the detailed characterization such as FTIR, XRD, FE-SEM, LC-MS, zeta-potential analysis, and particle size distribution. The obtained cytotoxicity data and hydrogen-bonding

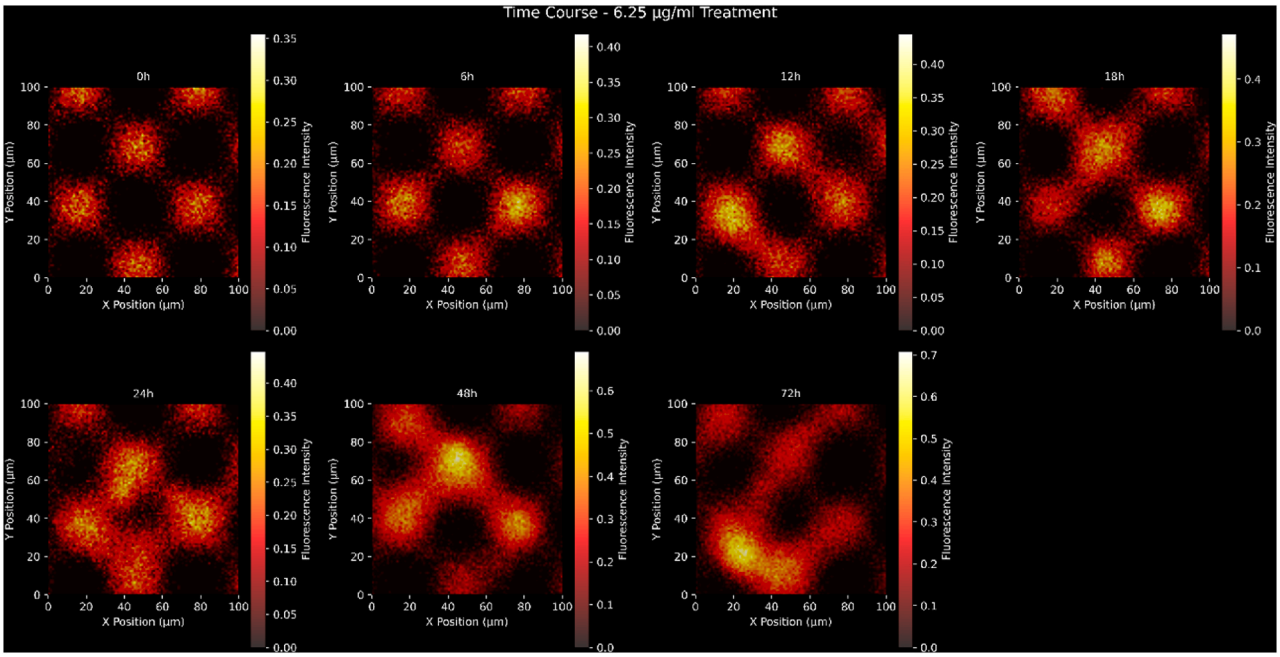

Fig. 27. Fluorescence intensity over time at various intervals (0h, 6h, 12h, 18h, 24h, 48h, 72h) following a 6.25 µg/ml treatment.

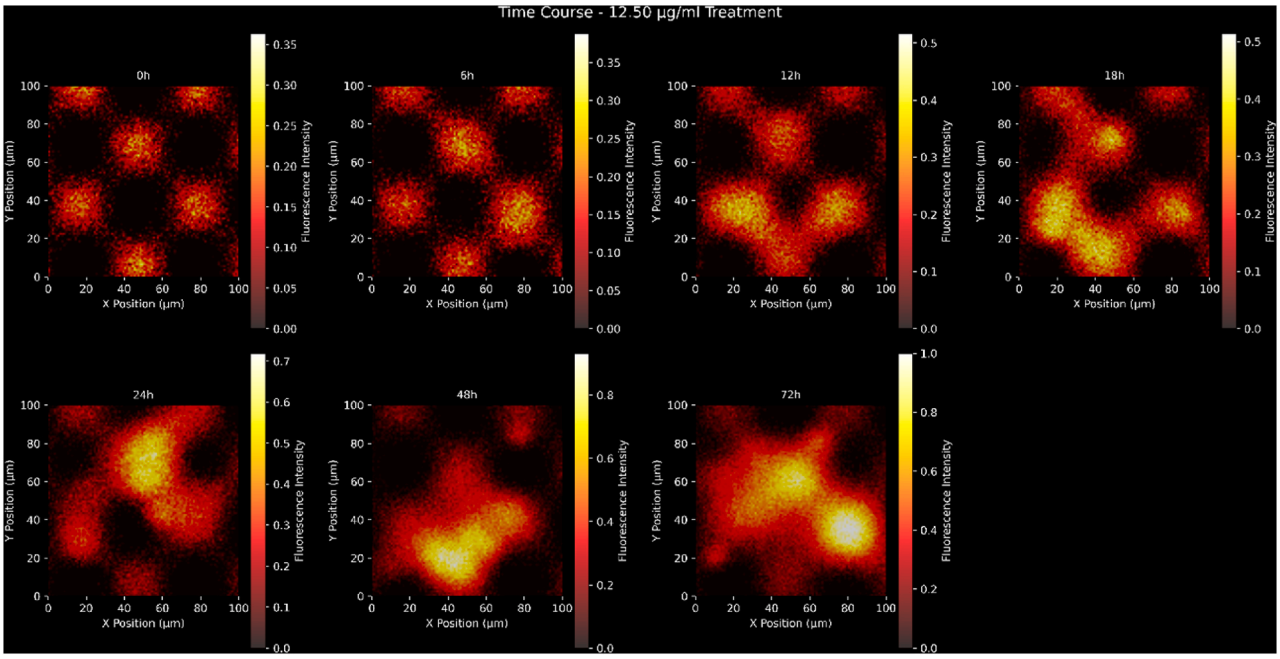

Fig. 28. Fluorescence intensity over time at various intervals (0h, 6h, 12h, 18h, 24h, 48h, 72h) following a 12.50 µg/ml treatment.

stability analysis support the biological interest and allow understanding better the molecular interactions of the anticancer activity of Eriodictyol.

To go on, the results of the research are very solid to warrant further preclinical investigations. The pharmacokinetic and biodistribution evaluations of Eriodictyol-SLNs in vivo that would identify systemic availability, metabolism and organ-based accumulation should be incorporated in future research. Xenograft or orthotopic animal model testing will be used to evaluate the efficacy of therapeutic benefits, the ability to induce tumour regression and survival. Mechanistic research assessing the number of apoptotic markers, PR pathways modulation, and downstream signalling (e.g., PI3K/Akt, NF-kB, p53) will also be used to confirm the computational predictions. The comparative study with the standard care treatments, including endocrine therapy with tamoxifen or aromatase inhibitors, can demonstrate the synergistic potential or dose-sparing effect. The in vitro cytotoxicity indicated that SLNs loaded with Eriodictyol possess good potential to inhibit the viability of cancer cells with IC_{50} of 37.2 µg/mL. These findings have shown that Eriodictyol has a high potential as an anticancer agent, particularly when the drug is delivered using a nanostructured platform. Unlike earlier reports, that generally explain the anticancer activity of Eriodictyol, in our report, machine-learning-based predictive target analysis, PR (−14.4 kcal/mol)-based high-affinity docking, MD-based experimentally valid interaction stability, and SLN-based

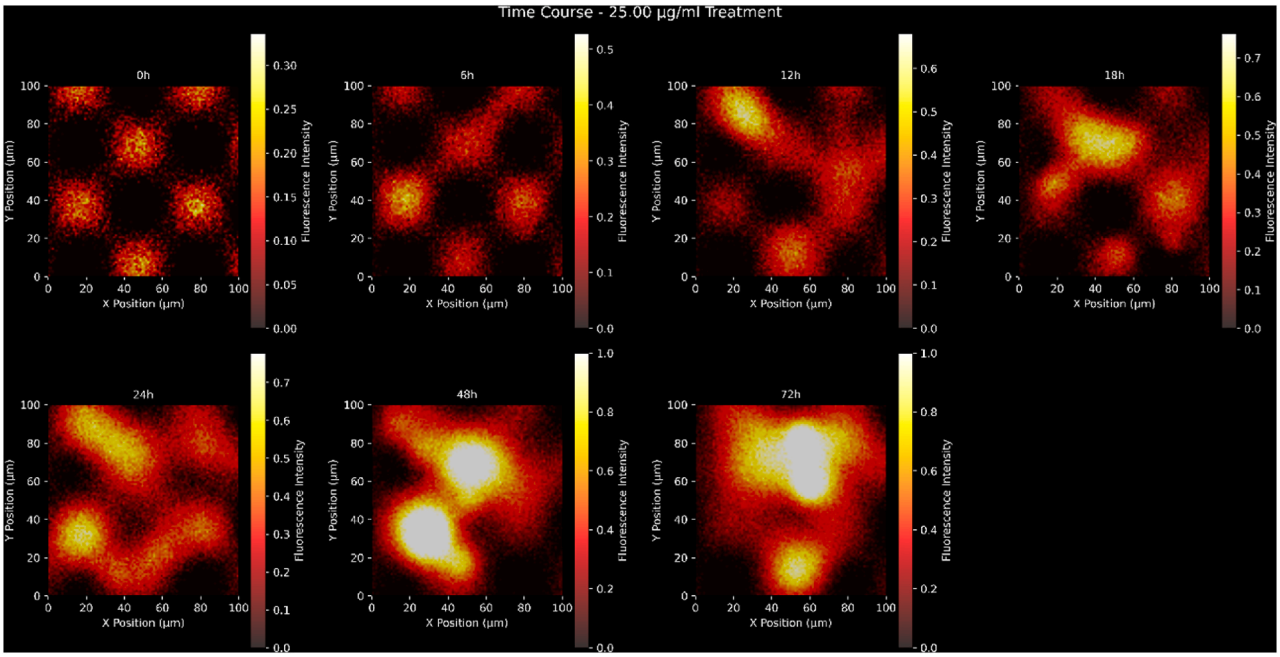

Fig. 29. Fluorescence intensity over time at various intervals (0h, 6h, 12h, 18h, 24h, 48h, 72h) following a 25 µg/ml treatment.

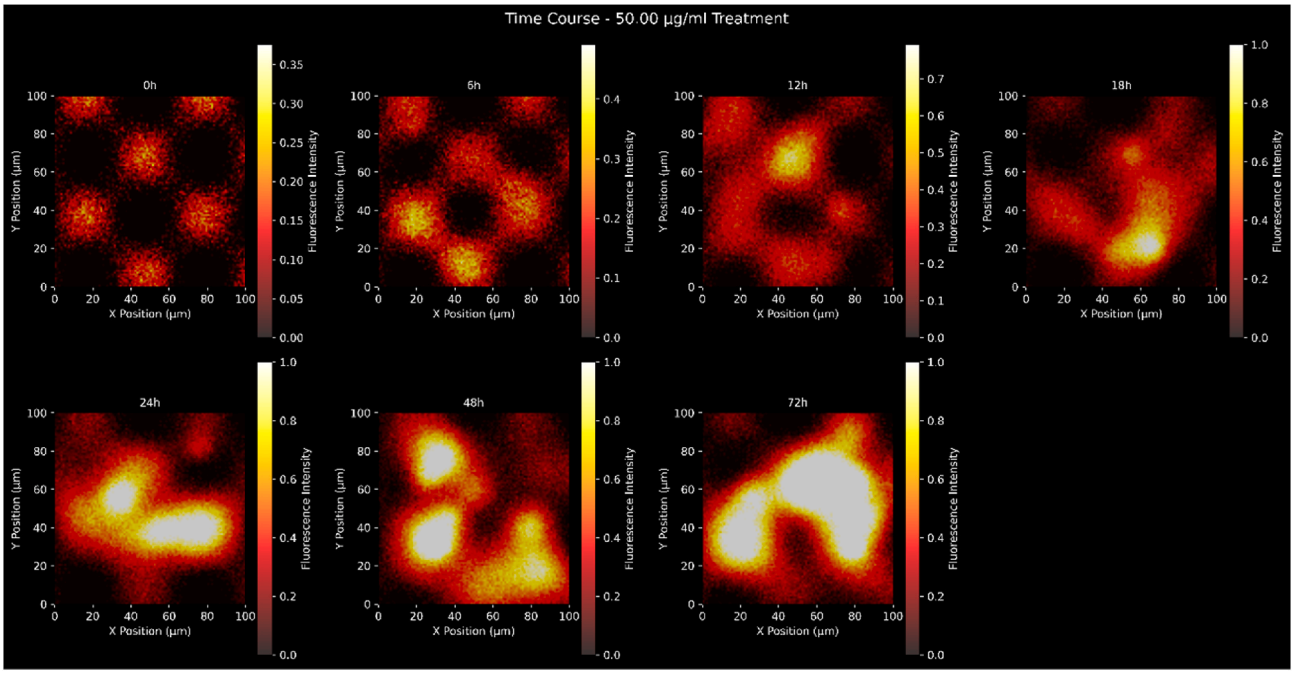

Fig. 30. Fluorescence intensity over time at various intervals (0h, 6h, 12h, 18h, 24h, 48h, 72h) following a 50 µg/ml treatment.

nanoformulation are combined with pH-responsive release and improved cytotoxicity, specifically in breast cancer. This computational and experimental approach forms a mechanistic delivery-driven progress which has not been described before in Eriodictyol which emphasizes its originality as a promising anti-breast-cancer treatment candidate. On the whole, this work forms a solid scientific and pharmaceutical basis of the development of Eriodictyol as a new, naturally based therapeutic and nano-enabled product. The unified model below gives us a roadmap on how to develop more infrastructures on clinically meaningful applications in the treatment of breast cancer.

CRediT authorship contribution statement

Salem Salman Almujri: Conceptualization, Methodology, Validation, Visualization, Writing – original draft, Writing – review & editing. **Prasanalakshmi Balaji:** Validation, Visualization, Writing – review & editing. **Kumarappan Chidambaram:** Validation, Visualization, Writing – review & editing. **Srinivasan Ramamurthy:** Validation, Visualization, Writing – review & editing. **Malarkodi Velraj:** Validation, Visualization, Writing – review & editing. **Swati Mayur Keny:** Validation, Visualization, Writing – review & editing. **A. Santhana Krishna Kumar:** Conceptualization, Methodology, Validation, Visualization, Writing – original draft, Writing – review & editing.

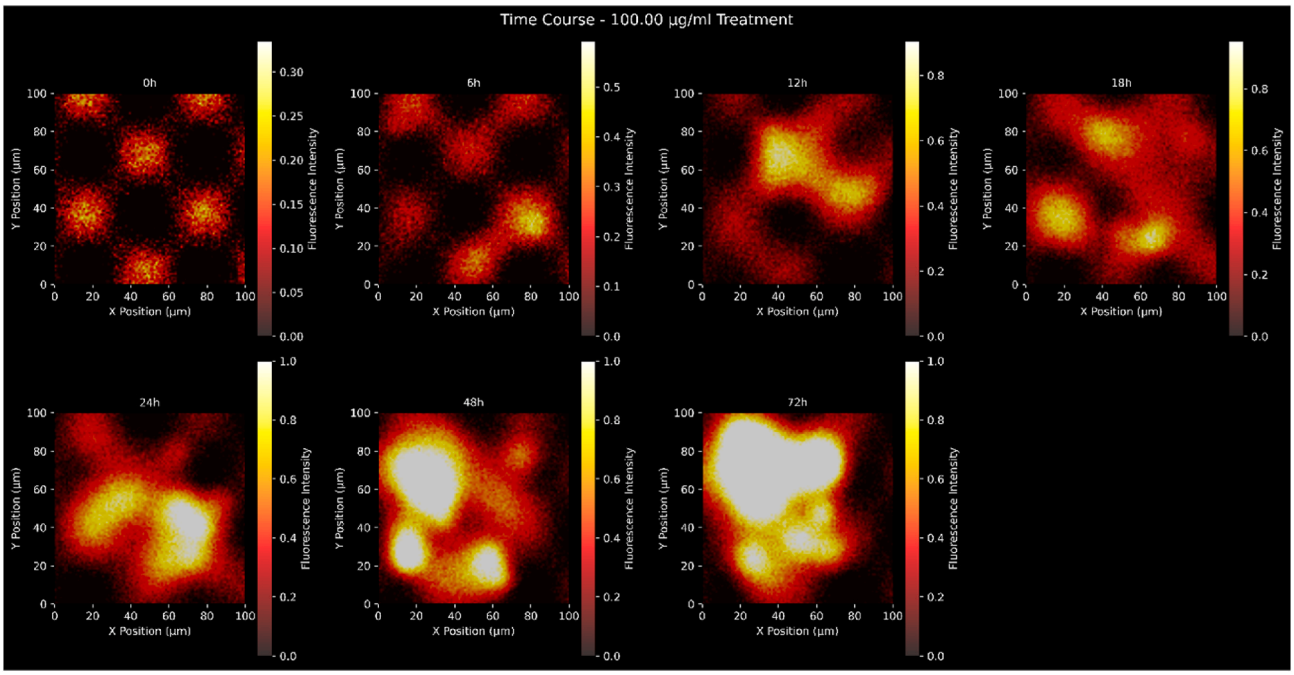

Fig. 31. Fluorescence intensity over time at various intervals (0h, 6h, 12h, 18h, 24h, 48h, 72h) following a 100 µg/ml treatment.

Panneerselvam Theivendren: Conceptualization, Methodology, Software, Validation, Visualization, Writing – original draft, Writing – review & editing.

Declaration statement

The authors declare that they have no known competing financial interests or personal relationships that could have appeared to influence the work reported in this paper.

Disclosure statement

All authors declare that there are no conflicts of interest associated with the publication of this manuscript.

Funding statement

We would like to thank and gratefully acknowledge the grants from NSTC to A. Santhana Krishna Kumar (NSTC 114-2221-E-110-007) for the financial support of this study and NSYSU-KMU Joint Research Project (NSYSU-KMU 115-P17) for the financial support of this study.

Declaration of competing interest

The authors declare that they have no known competing financial interests or personal relationships that could have appeared to influence the work reported in this paper.

Data availability

No data was used for the research described in the article.

References

[1] Chen, Y., Yu, D., Zhu, D., Muthusamy, S., Deshpande, M., Kiruthiga, N., Theivendren, P., Rajalakshmi, K., Wu, S., Zhu, C., 2025. Exploring alkaloids and flavonoids from natural sources: emerging natural agents for inhibiting cervical cancer progression through apoptosis induction, anti-inflammatory effects, and oxidative stress reduction. Pathol. Res. Pract., 156092

[2] Dinesh, B.G.H., Bandral, S.K., Sadashivappa, N.M., Ganjipete, S., Ammunje, D.N., Kunjiappan, S., Theivendren, P., Jays, J., Pavadai, P., 2025. Targeting the PI3K pathway: advancements and achievements in breast cancer therapy. Curr. Pharm. Des.

[3] Kunjiappan, S., Pavadai, P., Vellaichamy, S., Ram Kumar Pandian, S., Ravishankar, V., Palanisamy, P., Govindaraj, S., Srinivasan, G., Premanand, A., Sankaranarayanan, M., 2021. Surface receptor-mediated targeted drug delivery systems for enhanced cancer treatment: a state-of-the-art review. Drug Dev. Res. 82, 309–340.

[4] Pandian, S.R.K., Theivendren, P., Ravishankar, V., Pavadai, P., Vellaichamy, S., Palanisamy, P., Sankaranarayanan, M., Kunjiappan, S., 2022. Emerging Nanomaterials for Cancer Targeting and Drug Delivery, Engineered Nanomaterials for Innovative Therapies and Biomedicine. Springer International Publishing Cham, pp. 343–372.

[5] Radhakrishna, G.K., Ammunje, D.N., Kunjiappan, S., Ravi, K., Vellingiri, S., Ramesh, S.H., Almeida, S.D., Sireesha, G., Ramesh, S., Al-Qahtani, S., 2024. A comprehensive review of capsaicin and its role in cancer prevention and treatment. Drug Research 74, 195–207.

[6] Ramesh, S., Almeida, S.D., Hammigi, S., Radhakrishna, G.K., Sireesha, G., Panneerselvam, T., Vellingiri, S., Kunjiappan, S., Ammunje, D.N., Pavadai, P., 2023. A review of PARP-1 inhibitors: assessing emerging prospects and tailoring therapeutic strategies. Drug Research 73, 491–505.

[7] Surya, C., Lakshminarayana, A.B.V., Ramesh, S.H., Kunjiappan, S., Theivendren, P., Kumar, A.S.K., Ammunje, D.N., Pavadai, P., 2024. Advancements in breast cancer therapy: the promise of copper nanoparticles. J. Trace Elem. Med. Biol. 86, 127526.

[8] Theivendren, P., Gopalakrishnan, P., Sivakumar, A., Pachiappan, S., Chimakurthy, J., Murugavel, A., 2025. Utilization of Camellia sinensis as a STAT inhibitor in the management and prevention of breast cancer: a review. Pharmacological Research-Natural Products, 100375.

[9] Theivendren, P., Kunjiappan, S., Hegde, Y.M., Ravi, K., Vellaichamy, S., Gopal, M., 2022. The future perspectives of drug repurposing and treatment for the drug resistant breast cancer. Drug Repurposing: Molecular Aspects and Therapeutic Applications 139.

[10] Theivendren, P., Kunjiappan, S., Pavadai, P., Shanmugam, A., Karunanithi, K., Gopal, M., Kiruthiga, N., 2025. Success Stories: Impactful Applications of Cancer Biomarkers, the Potential of Cancer Biomarkers. Elsevier, pp. 297–331.

[11] Theivendren, P., Narayanasamy, P., Chidamabaram, K., Menon, S., Sahayaraj, J.A. D.A., Kiruthiga, N., Pandiyan, B., 2025. In-Depth Review of Breast Cancer and Inflammation Pre-and Post-treatment Strategies with Conventional and Novel Steroid Agents. Advances in Biological Regulation, 101102.

[12] Theivendren, P., Pavadai, P., Kunjiappan, S., Ravi, K., Kiruthiga, N., Chidamabaram, K., Alagarsamy, S., Reddy, N.B., 2025. Emerging therapeutic strategies and opportunities in targeting protein pathways for breast cancer treatment: a critical review. Nanotechnology.

[13] Theivendren, P., Pavadai, P., Veerachamy, S., Palanisamy, P., Kunjiappan, S., 2025. Surface receptor-targeted protein-based nanocarriers for drug delivery: advances in cancer therapy. Nanotechnology 36, 122003.

[14] Bhattarai, K., Bhattarai, R., Pandey, R.D., Paudel, B., Bhattarai, H.D., 2024. A comprehensive review of the phytochemical constituents and bioactivities of *Ocimum tenuiflorum*. Sci. World J. 2024, 8895039.

[15] Hanumanthaiah, P., Panari, H., Chebte, A., Haile, A., Belachew, G., 2020. Tulsi (ocimum sanctum)–A myriad medicinal plant, secrets behind the innumerable benefits. Arabian Journal of Medicinal and Aromatic Plants 6, 105–127.
[16] Kasmara, D.P., Singarimbun, N.B., Perangin-Angin, S.A.B., 2024. *Ocimum tenuiflorum* linne: a narrative review. Int. J. N. Innovat. 3, 25–41.
[17] Zahran, E.M., Abdelmohsen, U.R., Khalil, H.E., Desoukey, S.Y., Fouad, M.A., Kamel, M.S., 2020. Diversity, phytochemical and medicinal potential of the genus Ocimum L.(Lamiaceae). Phytochem. Rev. 19, 907–953.
[18] Ijinu, T.P., Jacob, J., Sasikumar, P., Varghese, T., Nair, R.R., Pushpangadan, P., 2023. Phytochemical Constituents and Pharmacology of *Ocimum tenuiflorum* L, Bioactives and Pharmacology of Lamiaceae. Apple Academic Press, pp. 389–413.
[19] Jahanger, M.A., Patra, K.K., Kumari, S., Singh, A., Manika, N., Srivastava, R.P., Saxena, G., Singh, L., 2023. A glance at the phytochemical and ethno-pharmacological understanding of four Ocimum species. Curr. Pharm. Biotechnol. 24, 1094–1107.
[20] Ali, Z.M., Hassoon, N.H., Ahmed, W.S., Abed, H.N., 2020. The application of data mining for predicting academic performance using k-means clustering and naïve bayes classification. Int. J. Psychosoc. Rehabil. 24, 2143–2151.
[21] Chase, R.J., Harrison, D.R., Burke, A., Lackmann, G.M., McGovern, A., 2022. A machine learning tutorial for operational meteorology. Part I: traditional machine learning. Weather Forecast. 37, 1509–1529.
[22] Esaki, T., Yonezawa, T., Yamazaki, D., Ikeda, K., 2022. Prediction models for fraction of absorption and membrane permeability using mordred descriptors. Chem. Bio Inf. J. 22, 46–54.
[23] Janoudi, G., Uzun, M., Fell, D.B., Ray, J.G., Foster, A.M., Giffen, R., Clifford, T., Walker, M.C., 2024. Outlier analysis for accelerating clinical discovery: an augmented intelligence framework and a systematic review. PLOS Digital Health 3, e0000515.
[24] Liu, T., Hwang, L., Burley, S.K., Nitsche, C.I., Southan, C., Walters, W.P., Gilson, M. K., 2025. BindingDB in 2024: a FAIR knowledgebase of protein-small molecule binding data. Nucleic Acids Res. 53, D1633–D1644.
[25] Panneerselvam, T., Kunjiappan, S., Govindaraj, S., Gopal, M., Natarajan, K., Hegde, Y.M., Shanmugam, N., Srinivas, G., Ravi, K., Natarajan, V., 2022. Graph theoretical analysis, in silico modeling and molecular dynamic studies of (5-((2-chloropyridin-4-yl) oxy)-3-phenyl-1H-pyrazol-1-yl)-2-(4-substituted phenyl)-N, N-dimethylethen-1-amine derivatives for the treatment of breast cancer. Anti Cancer Agents Med. Chem.
[26] Rajeshkumar, R.R., Kumar, B.K., Parasuraman, P., Panneerselvam, T., Sundar, K., Ammunje, D.N., Pandian, S.R.K., Murugesan, S., Kabilan, S.J., Kunjiappan, S., 2022. Graph theoretical network analysis, in silico exploration, and validation of bioactive compounds from Cynodon dactylon as potential neuroprotective agents against α-synuclein. Bioimpacts: BI 12, 487.
[27] Saravanan, G., Panneerselvam, T., Kunjiappan, S., Parasuraman, P., Alagarsamy, V., Udayakumar, P., Soundararajan, M., Joshi, S.D., Ramalingam, S., Ammunje, D.N., 2019. Graph theoretical analysis, in silico modeling, prediction of toxicity, metabolism and synthesis of novel 2-(methyl/phenyl)-3-(4-(5-substituted-1, 3, 4-oxadiazol-2-yl) phenyl) quinazolin-4 (3H)-ones as NMDA receptor inhibitor. Drug Dev. Res. 80, 368–385.
[28] Kalimuthu, A.K., Parasuraman, P., Sivakumar, P., Murugesan, S., Arunachalam, S., Pandian, S.R.K., Ravishankar, V., Ammunje, D.N., Sampath, M., Panneerselvam, T., 2022. In silico, in vitro screening of antioxidant and anticancer potentials of bioactive secondary metabolites from an endophytic fungus (Curvularia sp.) from Phyllanthus niruri L. Environ. Sci. Pollut. Control Ser. 29, 48908–48925.
[29] Ilyas, M., Khan, M.A., Xiong, L., Zhang, L., Lauqman, M., Abbas, M., Zohaib, H.M., Manurkar, N., Li, H., 2025. Enhancements of the first and second hyperpolarizability of a GMP coordination polymer: crystal structure and computational studies. Dalton Trans. 54, 5921–5934.
[30] Kunjiappan, S., Govindaraj, S., Parasuraman, P., Sankaranarayanan, M., Arunachalam, S., Palanisamy, P., Mohan, U.P., Babkiewicz, E., Maszczyk, P., Vellaisamy, S., 2020. Design, in silico modelling and functionality theory of folate-receptor-targeted myricetin-loaded bovine serum albumin nanoparticle formulation for cancer treatment. Nanotechnology 31, 155102.
[31] Kunjiappan, S., Sankaranarayanan, M., Kumar, B.K., Pavadai, P., Babkiewicz, E., Maszczyk, P., Glodkowska-Mrowka, E., Arunachalam, S., Pandian, S.R.K., Ravishankar, V., 2020. Capsaicin-loaded solid lipid nanoparticles: design, biodistribution, in silico modeling and in vitro cytotoxicity evaluation. Nanotechnology 32, 095101.
[32] Mandhadi, J.R., Panneerselvam, T., Parasuraman, P., 2020. DESIGN, in silico modeling, toxicity study and synthesis of novel substituted semicarbazide derivatives of pyrimidine: an antitubercular agent. Curr. Bioact. Compd. 16, 294–301.
[33] Palanichamy, C., Pavadai, P., Panneerselvam, T., Arunachalam, S., Babkiewicz, E., Ram Kumar Pandian, S., Shanmugampillai Jeyarajaguru, K., Nayak Ammunje, D., Kannan, S., Chandrasekaran, J., 2022. Aphrodisiac performance of bioactive compounds from Mimosa pudica Linn.: in silico molecular docking and dynamics simulation approach. Molecules 27, 3799.
[34] Pandian, S.R.K., Pavadai, P., Vellaisamy, S., Ravishankar, V., Palanisamy, P., Sundar, L.M., Chandramohan, V., Sankaranarayanan, M., Panneerselvam, T., Kunjiappan, S., 2021. Formulation and evaluation of rutin-loaded solid lipid nanoparticles for the treatment of brain tumor. N. Schmied. Arch. Pharmacol. 394, 735–749.
[35] Almeida, S.D., Ramesh, S.H., Radhakrishna, G.K., Sireesha, G., Ramesh, S., Kumar, B.S., Hosur Dinesh, B.G., Ganjipete, S., Nagaraj, S., Theivendren, P., 2025. Development and evaluation of S-carboxymethyl-L-cystine-loaded solid lipid nanoparticles for Parkinson's disease in murine and zebrafish models. Sci. Rep. 15, 10885.
[36] Mubashar, I., Maroof Ahmad, K., Nagesh Manurk, fiz Muhammad, Z., Talha, B., Afsheen, S., Hui, L., 2025. Unravelling the impact of octahedral distortion and non…(II) and Ni(II) coordination complexes with uridine nucleotide. Mater. Today Chem. 47, 102818.
[37] Ferreira, M., Costa, D., Sousa, Â., 2022. Flavonoids-based delivery systems towards cancer therapies. Bioengineering 9, 197.
[38] Ranjbar, S., Emamjomeh, A., Sharifi, F., Zarepour, A., Aghaabbasi, K., Dehshahri, A., Sepahvand, A.M., Zarrabi, A., Beyzaei, H., Zahedi, M.M., 2023. Lipid-based delivery systems for flavonoids and flavonolignans: liposomes, nanoemulsions, and solid lipid nanoparticles. Pharmaceutics 15, 1944.